

University of New Hampshire
University of New Hampshire Scholars' Repository

Master's Theses and Capstones

Student Scholarship

Spring 2017

Performance Evaluation of the Velodyne VLP-16 System for Surface Feature Surveying

John Ryan Kidd

University of New Hampshire, Durham

Follow this and additional works at: <https://scholars.unh.edu/thesis>

Recommended Citation

Kidd, John Ryan, "Performance Evaluation of the Velodyne VLP-16 System for Surface Feature Surveying" (2017). *Master's Theses and Capstones*. 1116.

<https://scholars.unh.edu/thesis/1116>

This Thesis is brought to you for free and open access by the Student Scholarship at University of New Hampshire Scholars' Repository. It has been accepted for inclusion in Master's Theses and Capstones by an authorized administrator of University of New Hampshire Scholars' Repository. For more information, please contact nicole.hentz@unh.edu.

PERFORMANCE EVALUATION OF THE VELODYNE VLP-16 SYSTEM FOR
SURFACE FEATURE SURVEYING

BY

John Ryan Kidd, LT/NOAA

Ocean Earth and Atmospheric Sciences BS, Old Dominion University, 2010

THESIS

Submitted to the University of New Hampshire

in Partial Fulfillment of
the Requirements for the Degree of

Master of Science

in

Earth Sciences: Ocean Mapping

May, 2017

This thesis has been examined and approved in partial fulfillment of the requirements for the degree of Master of Science in Earth Sciences: Ocean Mapping by:

Thesis/Dissertation Director, Shachak Pe'eri, Research Associate Professor

Andrew Armstrong, Co-Director, Joint Hydrographic Center, Affiliate Professor

Dr. Firat Eren, Center for Coastal and Ocean Mapping, Research Scientist II

On April 6, 2017

Original approval signatures are on file with the University of New Hampshire Graduate School.

Acknowledgements

A special thanks to Vitad Pradith from HYPACK® for assisting with the integration of the VLP-16 laser scanner on a marine survey vessel, Frank Bertini and David Oroshnik from Velodyne LiDAR™ for providing their technical expertise, Paul Lavoie for his flexibility and assistance with fabricating various laser scanner mounts, Ben Smith, Emily Terry, and Dan Tauriello for expertly navigating the R/V Coastal Surveyor and R/V Gulf Surveyor in the challenging near-shore environment of Portsmouth Harbor, the Piscataqua River, and the New Hampshire shoreline. Additionally, I would like to thank Matt Birkebak and Rabine Keyetieu for help with data collection and experimental design.

Table of Contents

Acknowledgements.....	iii
List of Tables	vi
List of Figures	vii
Abstract.....	xi
1. Introduction	1
Background.....	1
Potential Solution	4
Proposition	6
2. Terrestrial Laser Scanners.....	8
Terminology.....	8
Range Estimation.....	10
Laser Beam Characteristics.....	11
Target Detection.....	13
Scanning Mechanism.....	14
Integration of TLS Systems into Survey Vessels	15
Scanning System Geometry (Reference Frames)	17
3. Methodology.....	20
International Hydrographic Organization (IHO) S-44 Standards	20
Experimental Apparatus	22
UNH wave and tow tank in Chase Engineering Lab	22

UNH Judd Gregg Marine Research Complex and R/V Gulf Surveyor	22
Alignment	23
Laser Beam Orientation	26
Estimating Range Uncertainty.....	29
Data Density	31
 4. Results.....	36
Laser Beam Orientation.....	36
Estimating Range Uncertainty	42
Data Density	52
 5. Discussion.....	59
Field Operations	59
Vegetation and Surface Ripples	59
Bridges and Overhead Power Cables	62
Compliance with IHO's S-44 Standards	66
Future Directions	68
 6. Conclusions	70
References	72

List of Tables

Table 2.1: Key parameters which describe or affect laser scanner performance.....	9
Table 2.2: Velodyne VLP-16 specifications (Velodyne LiDAR 2015).....	16
Table 2.3: A comparison of four laser scanning systems considered by NOAA.	17
Table 3.1: IHO Minimum standards for hydrographic surveys (IHO, 2008)	21
Table 3.2: Acquisition vessel, R/V Gulf Surveyor	23
Table 4.1: Measured offsets from mechanical calibration and deviations from expected angle..	40
Table 4.2: Elevation angular uncertainty at 2σ CI.....	42
Table 4.3: Results of the point count within a 1 m^2 window from the data density simulation ..	54
Table 4.4: Tabular results of the point count within a 1m^2 box from the field validation experiment.....	56
Table 4.5: Percent error between theoretical (computer simulation) and experimental (field validation). Small numbers represent a good comparison and large numbers represent a poor comparison.....	57
Table 5.1: Charted vs. surveyed vertical clearances of overhead features surveyed within Portsmouth Harbor, NH. Difference = charted - surveyed	66

List of Figures

Figure 2.1: Range estimations based on time-of-flight measurements. A_T and A_R are the amplitudes of the transmitted laser and received laser, respectively.	10
Figure 2.2: Signal-to-noise illustration. A_T and A_R are the amplitudes of the transmitted laser and received laser, respectively.	13
Figure 2.3: Relationship between a laser scanner on a marine survey platform and a geographic reference system. Modified from Habib et al. 2010.	18
Figure 3.1: Illustration of experiment set-up with laser scanner's reference frame (side view) ...	25
Figure 3.2: A 1-inch wide strip of aluminum used as an alignment target. The strip is vertically mounted to a rigid frame.....	25
Figure 3.3: Conversion from spherical coordinates to Cartesian coordinates.	26
Figure 3.4: VLP-16 laser scanner mounted above a high precision rotating compass.	27
Figure 3.5: Relative reference frames were established on the -11° , -3° , $+3^\circ$, and $+11^\circ$ beams to cover the $\pm 15\text{deg}$ window of the scanner. From each of these reference frames, the four surrounding laser beams were verified.	28
Figure 3.6: Hypothetical intensity returns, centered around the $+5^\circ$ beam, from rotating the scanner by increments of 0.04° through a window of $\pm 0.24^\circ$ centered on the assumed location of the laser beam.	29
Figure 3.7: Four targets used for estimating ranger uncertainty. From left to right; whiteboard, wood, concrete, and sand.	30
Figure 3.8: Experiment setup with laser scanner setup vertically on tripod at edge of the tow tank and the target mounted to the tow carriage at 10 m range.	30

Figure 3.9: Clipped data resulting from an azimuth window filter. Left- before filtering. Right- after filtering.	31
Figure 3.10: Top down view of geometric computer simulation where R is the range from the scanner to the planar target.	32
Figure 3.11: Target for the data density experiment was a vertical flat and relatively smooth area of the UNH pier-face. Left: A side view of the pier-face. Right: Top-down view of data on pier-face from one pass.	34
Figure 3.12: Northeast to southwest lines from 10-100 m. Purple box is the target of interest. Not drawn to scale.	34
Figure 3.13: Example of data density within a 1 m^2 box, normal vector shown.	35
Figure 4.1: Angular separation measured with respect to the four neighboring beams with a reference frame established on the -11° beam.	38
Figure 4.2: Angular separation measured with respect to the four neighboring beams with a reference frame established on the -3° beam.	38
Figure 4.3: Angular separation measured with respect to the four neighboring beams with a reference frame established on the $+3^\circ$ beam.	39
Figure 4.4: Angular separation measured with respect to the four neighboring beams with a reference frame established on the $+11^\circ$ beam.	39
Figure 4.5: Scatterplot of deviations from expected angle for each beam.	41
Figure 4.6: Range measurements to a whiteboard target at various incident angles, where data points are colored by intensity and four black horizontal error bars represent the 2σ CI for each 2.5cm vertical bins.	43

Figure 4.7: Range measurements to a wood target at various incident angles, where data points are colored by intensity and four black horizontal error bars represent the 2σ CI for each 2.5cm vertical bins.....	44
Figure 4.8: Range measurements to a concrete target at various incident angles, where data points are colored by intensity and four black horizontal error bars represent the 2σ CI for each 2.5cm vertical bins.....	45
Figure 4.9: Range measurements to a sand target at various incident angles, where data points are colored by intensity and four black horizontal error bars represent the 2σ CI for each 2.5cm vertical bins.....	46
Figure 4.10: Oblique target and intersecting laser beam footprint.	47
Figure 4.11: Average 2σ CI for all targets.	48
Figure 4.12: Range uncertainty results extrapolated out to the maximum range of the laser scanner, 100 m.	49
Figure 4.13: Average 2σ CI on an aluminum strip of metal at a range of 8 m and normal incidence for all laser beams.....	50
Figure 4.14: Side-view of the range bias observed due to oversaturated data points with respect to intensity within the specular area of the target.	51
Figure 4.15: Data density simulations for targets at 10 m (left), 50 m (center) and 100 m (right) using 5 Hz (top) and 20 Hz (bottom) scanning rates with the scanner mounted vertically. The blue window represents the 1 m^2 target used to estimate data density.	53
Figure 4.16: Data density simulations for targets at 10 m (left), 50 m (center) and 100 m (right) using 5 Hz (top) and 20 Hz (bottom) scanning rates with the scanner mounted at an oblique 45deg angle. The blue window represents the 1 m^2 target used to estimate data density.....	53

Figure 4.17: Data density results within a 1 m^2 window (marked in blue) at a range of 20m, scanner rotation rate of 5 Hz with a vertical scanner mounting orientation. The blue line represents the normal vector from the plane-of-best-fit used to align the box and plane of data.	55
Figure 5.1: Whaleback Lighthouse at the entrance to Portsmouth Harbor. Scanning range to lighthouse was approximately 70 m.	61
Figure 5.2: Rocky islet at the entrance of Portsmouth Harbor. Scanning range to right-most rock was approximately 64 m.	61
Figure 5.3: Pilings and floating pier near Fort Point, NH.	61
Figure 5.4: Memorial Bridge within Portsmouth Harbor. Scanning range to bottom of bridge span was approximately 60m.	63
Figure 5.5: Sarah Mildred Long Bridge within Portsmouth Harbor. Scanning range to top of the pillars was approximately 75m.	63
Figure 5.6: I-95 bridge within Portsmouth Harbor. Scanning range to the bottom of the bridge span was approximately 60m.	63
Figure 5.7: Overhead power cables stretching across Back Channel area within Portsmouth Harbor. Range to cables was approximately 16m.	64
Figure 5.8: Overhead power cables stretching across the main channel just north of the I-95 bridge within Portsmouth Harbor. Range to cables was approximately 60m.	64

Abstract

PERFORMANCE EVALUATION OF THE VELODYNE VLP-16 SYSTEM FOR SURFACE
FEATURE SURVEYING

By

LT John R Kidd, NOAA

University of New Hampshire, May, 2017

For safety of marine navigation, it is important to locate, describe, and chart the horizontal position and vertical elevation of exposed marine surface features such as piers, piles, and rocks. Vessel-mounted laser scanners have been previously demonstrated to be effective tools for this task. However, the use of expensive survey-grade laser scanners for this shoreline survey requirement has been considered by United States charting authorities to be cost prohibitive. In this work, an in-depth performance evaluation of the Velodyne VLP-16 system, a low-cost industrial-grade mobile laser scanner, was conducted to characterize its performance. The VLP-16's accuracy of range estimates as a function of distance and angle of incidence, angular separation between individual beams, and data density as a function of mounting orientation and scanner settings were measured and assessed. The uncertainties of these key parameters were derived through multiple experiments under both well-controlled laboratory and realistic field conditions. The results of the study demonstrate that the use of low-cost industrial-grade mobile laser scanners can be a cost-efficient survey tool for mapping marine surface features with performance that can meet survey requirements for charting purposes. Additionally, this study demonstrates that the Velodyne VLP-16 can be used as a validation tool for measuring the vertical clearance of bridges and overhead power cables crossing navigation channels.

1. Introduction

Background

The National Oceanic and Atmospheric Administration (NOAA) Office of Coast Survey (OCS) provides up-to-date nautical charts and other navigational products and services to promote safe and efficient maritime commerce along the United States inland and coastal waterways. NOAA charts and services are used by professional and recreational mariners alike to aid in the decision-making process for safely operating their vessels in proximity to hazards along the shoreline. These navigational charts depict both submerged and surface (exposed) features that may be along the mariner's intended navigation path. The United States Coast Guard (USCG) places man-made structures to serve as visual aids to navigation (AToNs) near many features that pose a significant threat to surface navigation as. Not all dangers, however, are marked with AToNs, and it is not uncommon for a buoy to be dragged from its mooring or a lighthouse to experience damage that can render the aids useless to mariners. In the absence of visual AToNs, the mariner's only means of obtaining the amount of detail concerning the local hazards to navigation is by consulting a navigational chart.

NOAA's National Geodetic Survey (NGS) Remote Sensing Division (RSD) is responsible for mapping the 95,000 miles of United States' shoreline as compiled from 1:80,000-scale charts (Parrish 2012). The shoreline mapping includes the intersection of the land-water interface at Mean High Water (MHW) and the attached anthropogenic land features exposed at MHW. In addition to the contiguous shoreline and attached features, mapping the nearshore non-

contiguous natural features, such as rocks, reefs, islets, and islands and anthropogenic features, such as piers, pilings, and bridges are also within RSD's scope of work (NOS, 2016). Whenever practicable, RSD also maps the intersection of the land-water interface at Mean Lower Low Water (MLLW) and features that may be exposed in the area between MHW and MLLW. These surveys are conducted by using remote sensing techniques aboard aircraft flying at relatively low altitudes. Ground truth observations are not part of this primary shoreline mapping process.

In most current NOAA hydrographic surveys with a nearshore component, NOAA's OCS field units are tasked to complete a limited shoreline verification survey of both anthropogenic and natural non-contiguous features to ensure that both source and charted datasets are accurate and are appropriately depicted on paper Raster Navigational Charts (RNCs) and digital Electronic Navigational Charts (ENCs). To complete the shoreline verification survey, small skiffs and/or hydrographic survey launches are deployed to verify or update the metadata associated with existing features, to disprove the existence of erroneously charted features or those that have weathered away, and to find and fully attribute metadata associated with previously undetected and uncharted features. Due to the draft limitations of the survey vessel and, most importantly, the safety of the survey crew, the inshore limit of feature verification is established by what NOAA designates as the Navigable Area Limit Line (NALL). The NALL is defined as the most seaward of three independent metrics: 1) the surveyed 4-meter depth contour, 2) the line defined by a distance equal to 0.8 millimeters at the largest scale chart seaward from the observed MHW line, or 3) the inshore limit of safe navigation for the survey vessel determined by the field party conducting the survey (NOS 2016). This means that while not every rock or feature near the

shore will be mapped, a set of features along the boundary between safe water and dangerous nearshore water must be accurately mapped.

Traditionally, NOAA surveyors are equipped for this task with pencil and paper for feature annotation, hand-held magnetic compasses and laser range finders for horizontally positioning targets relative to the survey vessel, discrete point positioning software (CARIS Notebook) with a backpack mounted global positioning system (GPS), and digital cameras (Wyllie et al. 2012). Due to the inherently dangerous nature of navigating a small vessel within a potentially poorly charted area, it is not uncommon for the NALL to be most limited by the surveyor's determination of the inshore limit of safe navigation.

When the survey team is deployed on small skiffs, a common practice is to approach the point feature of interest, such as an exposed rock, and extend the GPS antenna over the feature by using a pole. This method generally yields a more accurate horizontal position estimate as compared to the 'range and bearing' method of using a laser range finder and magnetic compass (Brennan et al. 2008). The result is a single measurement with a horizontal uncertainty on the order of 1 meter. A drawback of this approach is that the survey vessel is required to be stationary, which increases survey time and can pose a risk to the crew and equipment due to the potential of grounding, striking the object, or loss of boat stability due to wave action interacting with the inherently shallow bottom. Another common practice is to approach the feature with the antenna positioned on the bow of the small skiff while continuously logging the trackline using the GPS and acquisition software. Once the coxswain has navigated as closely to the feature as safely possible, the skiff retreats along the same trackline by putting the engine in

reverse. The result is a trackline with a discrete vertex that is considered to be the horizontal position of the feature. The uncertainty of this method depends upon how closely the skiff is able to approach the feature. The methods described above all provide an approximation of the location of the feature that may have an uncertainty no better than 1 meter, and in every case, the height of the feature can only be estimated by the surveyor. In cases of limited resources or logistical limitations, the survey of a feature is estimated by “*best means available*” which may potently involve more subjective methods, such as visual estimation of the target’s location and height above the water surface (NOS 2016). These ‘*best means available*’ approaches contain a large amount of uncertainty that degrade the quality of the deliverable and subsequently limit the value of the chart. It is clear that a safer, time efficient, and more accurate method is needed.

Potential Solution

An alternative approach for conducting shoreline verification surveys is to use a laser scanner that is integrated into the survey axillary sensors aboard a marine survey vessel. This approach allows the operator to conduct a dynamic survey from a safe distance from the target. The product from a terrestrial laser scanner (TLS) survey is a high-accuracy 3D point cloud with measurements on the order of centimeters of precision. Over the past decade, NOAA has conducted two evaluation projects using long-range (maximum detection greater than 100 m) survey-grade TLS systems.

In 2007, an evaluation survey was conducted aboard the NOAA vessel *Bay Hydrographer II*. This study tested a combination of videogrammetry and Riegl survey-grade laser scanner along with a long range Riegl LMS-Z420i 3D mobile laser scanner within the Inner Norfolk Harbor,

Virginia (Brennan et al. 2008). During the spring and summer of 2011, the NOAA Ship *Thomas Jefferson* and NOAA Ship Fairweather experimented with the Applanix™ LANDMark™ mobile laser scanner within the Inner Norfolk Harbor in Norfolk, VA and Woman’s Bay in Kodiak, AK, respectively (Wyllie et al. 2012). In both studies, the laser scanners exceeded performance expectations and greatly minimized the time required to complete a survey of shoreline features when compared to traditional methods. The studies also showed that shoreline surveys completed with a mobile laser scanner were able to find and fully attribute the metadata for many more uncharted features that would be considered unsafe to approach or too time-consuming to survey using traditional methods. However, these survey grade laser scanner systems were considered to be cost-prohibitive for this application, with an approximate cost of \$80,000-\$120,000 per system.

Others have also successfully demonstrated mobile laser scanning technologies aboard marine survey vessels. In 2008, the Port of London Authority and NetSurvey Limited conducted a combined high resolution survey by concurrently collecting bathymetry data from a Reson 7125 multibeam echosounder (MBES) and elevation data from a Riegl Z240i survey-grade mobile laser scanner (Mallace and Dillon-Leetch 2008). Similar to the NOAA evaluations, the survey-grade laser scanner was successfully integrated to provide engineering project support by delivering easily interpretable products and minimizing the amount of time needed to complete the survey. These systems are in operational used by a number of organizations for highly specialized mapping applications in which their cost is overcome by the value they provide.

Proposition

With the availability of Velodyne's (and other manufacturer's) low-cost industrial-grade laser scanners, a preliminary evaluation was conducted on a Velodyne HDL-32E scanner by the Joint Hydrographic Center / Center for Coastal and Ocean Mapping (JHC/CCOM) in collaboration with hydrographic software provider Hypack, Inc. (Pradith et al. 2015). This work successfully evaluated the ability of the scanner to interface the laser measurements with a vessel's auxiliary global navigation satellite system (GNSS) and inertial navigation system (INS) by using HYPACK's HYSWEEP software module. The goal of this thesis study is to establish the technical system performance characteristics and demonstrate a survey procedure using a laser scanner system mounted on a survey vessel for mapping surface features with accuracies that meet International Hydrographic Organization (IHO) S-44 standards. The system investigated was a Velodyne VLP-16. In comparison to the Velodyne HDL-32E, Velodyne VLP-16 has half the laser channels, is smaller in size, and is lower priced. The work conducted in this study includes: 1) an independent assessment of the laser scanner's performance in estimating range, accuracy, data density, and the ability to detect various target materials in a well-controlled environment and 2) an evaluation of different survey configurations for detecting and characterizing surface features in field work. Experiments were performed in the Jere A. Chase Ocean Engineering Laboratory at the University of New Hampshire under controlled settings to characterize each of the laser scanner's performance parameters. Field work was conducted using the R/V Gulf Surveyor within Portsmouth Harbor, NH to validate the performance parameters and to evaluate various survey configurations. Based on this study, it is expected that the integration of a low-cost industrial-grade mobile laser scanner aboard NOAA's hydrographic fleet will drastically decrease the time needed to complete a standard shoreline survey, in

addition, it will maximize the safety of the crew and equipment and will meet the IHO uncertainty specification as a cost-effective solution.

2. Terrestrial Laser Scanners

Terminology

Before describing the performance evaluation of Velodyne VLP-16 system, it is important to describe the basic principles of Light Detection and Ranging (LiDAR) technology and how this technology is implemented in mobile laser scanning systems. The primary function of all laser scanners is to actively measure the distance between a known reference point within the sensor and a target that has been illuminated by the laser (Wehr 2008). LiDAR is categorized as an active remote sensing technology because it actively transmits an electromagnetic pulse of energy (in the optical range) used to measure distance. While there is an abundant list of specific applications where this technology can be utilized (e.g., meteorology, air and water pollution, and grain-size analysis), it is most often used to create high-resolution 3D point-clouds describing terrain and objects (Bunkin and Voliak 2001 ; Kovalev 2004). Elevation models from these point clouds are used to perform navigation, emergency inspections, and engineering calculations at a high degree of accuracy (mm- to cm- scale) (Maune 2007). The design of all scanning LiDAR systems (terrestrial, atmospheric, topographic, or bathymetric) is similar in general (Bunkin & Voliak, 2001; Feygels et al., 2017; Measures, 1992; Renslow, 2012; Wehr, 2009). All systems require a laser transmitter, a scanning mechanism, a narrow band filter matched to the laser wavelength, and a detector. In this study, key parameters that describe or affect the performance of a terrestrial laser scanner system are grouped based on performance metrics used by the laser scanner: Laser Beam Characteristics, Target Detection, Scanning Mechanisms, and Range Estimation. Key parameters of a laser scanner system that describe or affect system performance are shown in Table 2.1 (Baltsavias 1999).

Parameter	Symbol	Description
Speed of light (m/s)	c	Refractive index of air ~1.0003, c=299,792,458 m/s
Maximum range (m)	R _{max}	Maximum unambiguous range of the scanner
Range resolution (m)	ΔR	The maximum range between two targets at which a single laser pulse can detect two targets separately
Scanning rate (Hz)	f _{sc}	The rate (cycles/second) at which the scanner rotates 360°
Field of view (deg)	FOV	The swath width of the laser scanner in angular units
Laser wavelength (nm)	λ	The transmitted laser wavelength of the TLS
Pulse energy (Joule)	$\langle Q \rangle$	Average energy of a single laser pulse
Pulse duration (ns)	t _p	The length of time the laser is emitting energy for a single pulse
Aperture of laser (m)	D	The diameter width of the laser aperture
Beam divergence (rad)	γ	The laser beam's angle of expansion
Laser footprint (cm²)	A _L	The area of the laser beam footprint at a given range
Pulse repetition rate (kHz)	PRR	The number of laser pulses transmitter per second
Reflectivity (unitless)	ρ	Reflectivity of a target, commonly expressed as a percentage
Azimuth angle (deg)	α	The horizontal angle from the scanner's 0° encoder
Elevation angle (deg)	β	The vertical angle from the scanners horizon
Swath Width (m)	SW	The swath width of the laser scanner in ground distance units

Table 2.1: Key parameters which describe or affect laser scanner performance

Range Estimation

The simplest form of range calculations that LiDAR technology uses is time-of-flight (TOF) that measures the time it takes for a laser pulse to travel from an emitter, to reflect off of a target, and to be received by a sensor. Equation 2.1 and Figure 2.1 describe and illustrate the TOF calculation, where Δt is the time difference and c is the speed of light (Wehr and Lohr 1999).

The time difference, Δt , is calculated using a counter that is activated using a photodetector. The counter starts and stops at triggered thresholds by a transmit amplitude, A_T , and receive amplitude, A_R , respectively. For example, the trigger threshold could be the leading edge of the pulse at which the signal voltage has reached a pre-determined value or at a specific fraction of the signal peak (Baltsavias 1999).

$$\text{Equation 2.1 : } R = \frac{1}{2}c * \Delta t$$

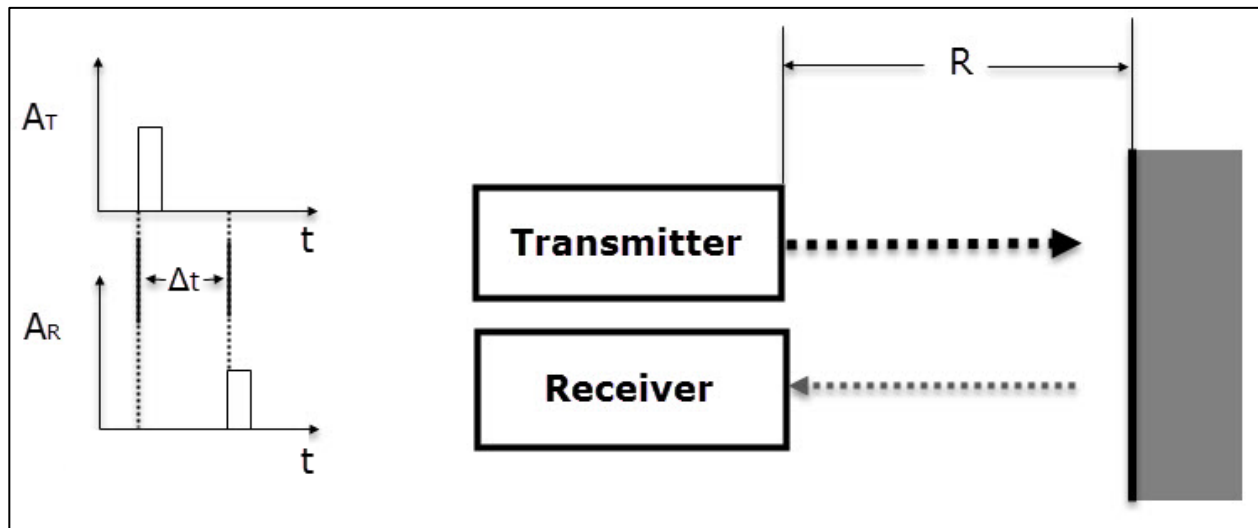


Figure 2.1: Range estimations based on time-of-flight measurements. A_T and A_R are the amplitudes of the transmitted laser and received laser, respectively.

Laser Beam Characteristics

Laser beam characteristics, such as laser wavelength, pulse energy, pulse duration, and beam divergence, depend on the desired application and the environmental medium. For example, while infrared wavelength (e.g. 1064 nm) is suitable for terrestrial surveys, green wavelength (e.g. 532 nm) is more suitable for bathymetric surveys due to water penetration capability. In order to commercialize a terrestrial laser scanner, the system needs to meet Occupational Safety and Health Administration (OSHA) standards that require all laser systems operating in outdoor environments to be below the maximum permissible exposure (MPE) safe under all conditions of normal use (OSHA 2016). The MPE value is determined by the average incident power over the area of the laser beam footprint (Equation 2.2).

$$\text{Equation 2.2: } MPE \geq \frac{\langle Q \rangle * PRR}{A_L}$$

Commercial terrestrial laser scanners typically utilize wavelengths that are within the near-infrared band (NIR) of the electromagnetic spectrum (750-1550 nm) that meet eye safety regulation and are characterized with a relative higher atmospheric transmission abilities (Baltsavias 1999). Common wavelengths used in terrestrial laser scanners are 900 nm and 1550 nm (emitted by semiconductor lasers and flashlamps) and 1064 nm (emitted by diode pumped solid state neodymium-doped yttrium aluminum garnet; Nd:YAG) lasers (Wehr 2008). While the energy at these wavelengths are eye safe and may pass through transparent and semi-transparent targets such as windows, IR radiation is so severely attenuated by water that it typically yields very little penetration, if at all (Measures 1992).

After a laser beam is generated by the transmitter unit, it often passes through a collimator, an optical device designed to more closely align then light rays to parallel in order to achieve the smallest beam divergence, γ , and therefore smallest beam footprints, A_L , possible. Beam divergence can be estimated by using Equation 2.3, where D is the aperture diameter (Wehr 2008)(Baltsavias 1999).

$$\text{Equation 2.3: } \gamma = 2.44 * \frac{\lambda}{D}$$

Given the beam divergence, the laser beam footprint can be estimated as a function of range using Equation 2.4, Equation 2.5, and Equation 2.6, where A_L is the area of the laser footprint, R is the range to the target, and D is the aperture of the laser (Baltsavias 1999):

$$\text{Equation 2.4: } A_L = D + 2R * \tan\left(\frac{\gamma}{2}\right)$$

Because D is considered small,

$$\text{Equation 2.5: } A_L = 2R * \tan\left(\frac{\gamma}{2}\right)$$

And because γ is considers small,

$$\text{Equation 2.6: } A_L = R * \gamma$$

Common beam divergence values for survey-grade and industrial-grade terrestrial laser scanners are 0.1 mrad and 3 mrad, respectively (Baltsavias 1999). The beam footprint diameters of both systems ranging to a target at a distance of 100 m are equal to 1 cm and 30 cm, respectively.

Target Detection

The ability of a laser scanner to detect a target is mostly determined by the signal-to-noise ratio (SNR) of the returning laser pulse which can be defined by the power ratio between the signal of the target within the laser return, P_{signal} , to the background noise present in the signal, P_{noise} , or the squared ratio of the target signal intensity, I_{signal} , and the intensity of the background noise, I_{noise} (Pe'eri 2015).

$$Equation\ 2.7:\ SNR = \frac{P_{signal}}{P_{noise}} = \left(\frac{I_{signal}}{I_{noise}} \right)^2$$

The minimum detectable object within the laser footprint does not depend on the object's size but primarily on its reflectivity (Baltsavias 1999). Consider a TLS that is capable of measuring the distance to a flat and even surface area, A, with a reflectivity of $\rho=5\%$. Then, the minimum area of a detectable object with a reflectivity $\rho=100\%$ at the same distance would be $A/20$ (Baltsavias 1999).

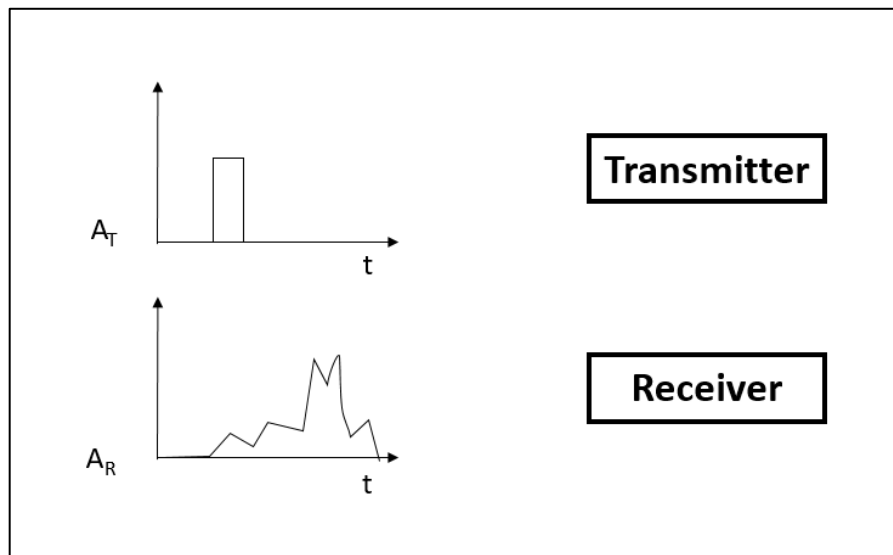


Figure 2.2: Signal-to-noise illustration. A_T and A_R are the amplitudes of the transmitted laser and received laser, respectively.

Other factors that affect the intensity of the returning laser signal include (Baltsavias 1999): range, laser power, atmospheric conditions, background irradiation, type of target reflectivity (i.e., diffuse, specular, or diffuse-specular mixing), terrain inclination, 3D shape of the target, laser aperture, detector sensitivity, noise level, and laser wavelength. It is important also to note that the energy of the pulse follows the Inverse Square Law, which states that the decreased energy is proportional to the inverse square of the distance (one-way transmission) shown in Equation 2.8. In the case of terrestrial laser scanners, the transmission is a two-way travel from the transmitter to the target and back.

$$\text{Equation 2.8: } \text{intensity} \propto \frac{1}{\text{distance}^2}$$

Small particles suspended in the air can cause laser returns that are strong enough to be considered a target. By far, the largest source of background noise is the scattering of the sunlight directly to the receiver or volume scattering caused by suspended water vapor (clouds, fog, or mist) or suspended particles (dust or smoke) (Baltsavias 1999).

Scanning Mechanism

The scanning patterns, pulse repetition rates, and multichannel characteristics of these scanners create extremely dense 3D point clouds. Most TLS have an opto-mechanical scanning device where an oscillating mirror or prism redirects the laser beam path in a precise controlled fashion to create a particular scanning pattern. Common scanning patterns include bi-directional z-shaped, rectilinear, circular, and elliptical (Baltsavias 1999). Scanning patterns affect only the distribution of the data. The two factors that affect data density are the Pulse Repetition Rate (PRR) of the laser emitter and the actual number of laser channels. The combination of PRR and

scanning rate, f_{sc} , create various data densities along the direction of scan angles. Maintaining the PRR while increasing the scanning rate will increase the point spacing. Conversely, maintaining the scanning rate while increasing the PRR will decrease the point spacing. Generally, scanners with more laser beams will generate larger datasets with greater point densities. Due to the relatively low-cost of the laser elements in industrial-grade laser scanners, these units often have multiple channels. For example, the Velodyne HDL-32E mobile laser scanner has 32 laser channels. Another difference between industrial grade laser scanners and survey-grade laser scanners is that the mechanical scanning device of the industrial systems does not use rotating mirrors or prisms.

Integration of TLS Systems into Survey Vessels

The Velodyne VLP-16 TLS was chosen as the sensor of interest due to its low cost, SWaP (size, weight and power), and its survey capabilities (Table 2.3). The VLP-16 system uses 16 lasers that scan 360° around a given axis. The scanner utilizes a 903nm infrared laser light, which is eye safe (Class I laser) and a reported range detection of up to 100 meters. The system is also reported to have an Ingress Protection (IP) rating of IP67 that allows the system to operate encapsulated in a sealed system making the unit able to withstand harsh environments (Velodyne LiDAR 2015). According to National Electrical Manufacturers Association (2004), the IP67 grade provided to the TLS system characterizes the systems as fully protected against contact (dust tight) with a reported test duration of up to 8 hours based on air flow and ingress of water in harmful quantity shall not be possible when the enclosure is immersed in water under defined conditions of pressure and time (up to 1 m of submersion).

Velodyne VLP-16 Specifications	
Sensor:	<ul style="list-style-type: none"> • Time of flight distance measurement with calibrated reflectivity • 16 channels • Measurement range 1 to 100m • Accuracy +/- 3 cm (typical) • Dual Returns (strongest and last) • Field of view (vertical): 30° (+15° to -15°) • Angular resolution (vertical): 2° • Field of view (horizontal/azimuth): 360° • Angular resolution (horizontal/azimuth): 0.1°-0.4° • Rotation rates: 5-20 Hz
Laser:	<ul style="list-style-type: none"> • Class 1 – eye safe • 903 nm wavelength (min/max is 896/910 nm) • Firing sequence repetition rate: 55.296 µs/18.2 kHz • Pulse duration: 6 ns • Maximum output energy: 31 Watts (0.19 micro Joules)
Mechanical/ Electrical/ Operational:	<ul style="list-style-type: none"> • Power consumption: 8 W (typical) • Operating voltage: 9-32 VDC (with interface box and regulated power supply) • Weight: 830 grams (without cabling) • Dimensions: 103 mm diameter x 72 mm height • Shock: 500m/sec² amplitude, 11 msec duration • Vibration: 5 Hz to 2000 Hz, 3G rms • Environmental protection: IP67 • Operating temperature -10° C to +60° C • Storage temperature -40° C to +105° C
Output:	<ul style="list-style-type: none"> • Data output: ~0.3 million points/second • 100 Mbps Ethernet Connection • UDP packets containing <ul style="list-style-type: none"> ◦ Distances ◦ Calibrated reflectivity ◦ Rotation angles ◦ Synchronized time stamps (µs resolution) • \$GPRMC NMEA sentence from FPS receiver

Table 2.2: Velodyne VLP-16 specifications (Velodyne LiDAR 2015)

Terrestrial Laser Scanner Comparison				
	<i>Velodyne VLP-16</i>	<i>Velodyne HDL-32</i>	<i>Riegl LMS-Z420i</i>	<i>Applanix LANDMark</i>
Grade	<i>Industrial</i>	<i>Industrial</i>	<i>Survey</i>	<i>Survey</i>
Price	\$8,000	\$29,900	\$80-200k	\$80-200k
Range	1 - 100m	1 - 100 m	2 - 1,000 m	3 - 1,700 m
Accuracy	$\pm 3\text{cm}$	$\pm 2\text{cm}$	10 mm	7 mm
Data Output	$\sim 300,000 \text{ pts/sec}$	$\sim 700,000 \text{ pts/sec}$	11,000 pts/sec	10,000 pts/sec
Laser Wavelength	<i>Near-infrared</i>	<i>Near-infrared</i>	<i>Near-infrared</i>	<i>Far- infrared</i>
Beam Divergence	3 mrad	2.79 mrad	0.25 mrad	0.150 mrad
Laser Class	<i>Class I</i>	<i>Class I</i>	<i>Class I</i>	<i>Class I</i>
Internal IMU	<i>N/A</i>	<i>MEMS</i>	<i>N/A</i>	<i>N/A</i>

Table 2.3: A comparison of four laser scanning systems considered by NOAA.

Scanning System Geometry (Reference Frames)

The VLP-16 system does not include internal auxiliary systems for navigation (e.g., Micro-Electro-Mechanical Systems, MEMS). Instead, the system is able to spatially reference itself by using the auxiliary navigation sensors that are typically available on survey vessels. The two auxiliary sensors used to reference the VLP-16 system include: 1) a global navigation satellite system (GNSS) that provides position and time synchronization between the TLS to the vessel's sensors and 2) an inertial measurement unit (IMU) which is used to derive the instantaneous orientations (roll, pitch, and yaw) and linear accelerations (surge, sway, and heave) of the vessel. Velodyne's VeloView and HYPACK's HYSWEEP module were used as both software interface between the laser measurements to the vessel's auxiliary systems and to time-synchronize the data stream coming from these different sensors.

Much like the solutions from airborne LiDAR systems (Gonsalves 2010), the coordinates of the multiple points from a laser scanner are derived by the integration of the solutions from the GNSS/IMU pair using HYPACK's HYSWEEP module. As a result, range, azimuth, and elevation angles of laser measurements are transformed from a local reference system (the origin of the scanner) to an earth-centered, earth-fixed (ECEF) reference frame, where the origin of the frame is the center of the Earth (Fossen 2011 ; Vanicek and Krakiwsky 1986). In order to properly transform the laser measurements, each sensor's mounting information with respect to the IMU (translational offsets and angular rotations) must be accounted for in the calculations.

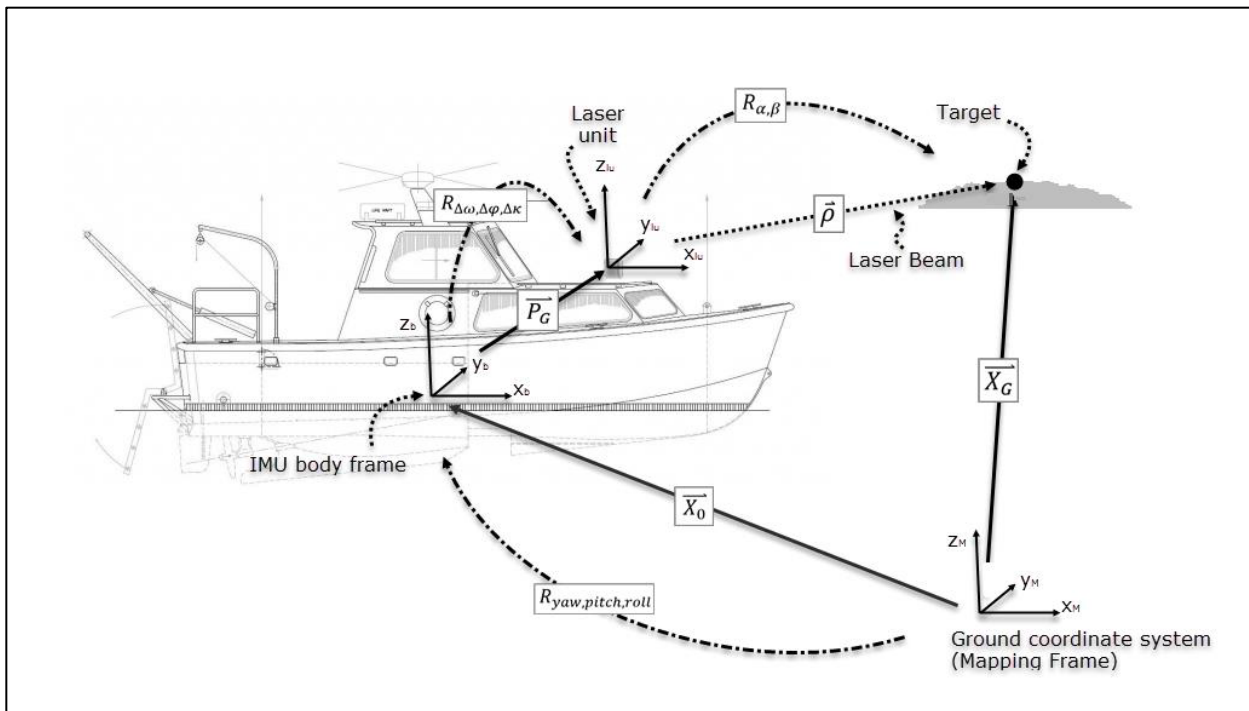


Figure 2.3: Relationship between a laser scanner on a marine survey platform and a geographic reference system. Modified from Habib et al. 2010.

The laser scanner geo-location equation, Equation 2.9, is based on the geo-location equation used in topographic airborne LiDAR systems (Habib et al. 2010).

$$\text{Equation 2.9: } \vec{X}_G = \vec{X}_0 + R_{yaw,pitch,roll} \vec{P}_G + R_{yaw,pitch,roll} R_{\Delta\omega, \Delta\phi, \Delta\kappa} R_{S_\alpha\alpha, S_\beta\beta} \begin{bmatrix} 0 \\ 0 \\ -\rho \end{bmatrix}$$

The three-dimensional position of the laser measurement, \vec{X}_G , is the sum of three ranges with the appropriate rotation matrixes applied. \vec{X}_0 represents the vector from the ground coordinate system to the origin of the IMU system. \vec{P}_G represents the vector from the origin of the IMU reference system to the laser scanner reference system. $\vec{\rho}$ represents the range vector from the laser scanner to the target lased. $R_{yaw,pitch,roll}$ is the rotation of the aircraft (measured by the IMU) with respect to the mapping frame. $R_{\Delta\omega, \Delta\phi, \Delta\kappa}$ is the boresight angles which relates the laser scanner reference system to the IMU reference system. $R_{\alpha,\beta}$ is the scan angle matrix, with α denoting the azimuth angle and β denoting the inclination angle. For the Velodyne VLP-16 laser scanner, the range of α is from 0° to 360° and the range of β angles is $\pm 15^\circ$ where $+15^\circ$ is above the scanner's horizon.

Although this study is using a marine survey vessel as the scanner's platform instead of an aircraft as presented by Habib et al., the mathematical foundations are the same. It is also important to note that all values for the LiDAR equation are measured in real-time with exception to the boresight angles, $R_{\Delta\omega, \Delta\phi, \Delta\kappa}$, the static lever arm between the IMU and laser scanner, \vec{P}_G , and the static lever arm between the primary GPS antenna and IMU.

3. Methodology

International Hydrographic Organization (IHO) S-44 Standards

As mentioned in the Introduction section, the main goal of this study is to develop and demonstrate a method to evaluate industrial-grade TLS systems for shoreline mapping applications in conjunction with hydrographic surveys. The capabilities of the Velodyne VLP-16 are investigated in this study because of NOAA's interest to integrate this system to auxiliary navigation systems that are already available on their hydrographic launches.

The IHO document S-44, Standards for Hydrographic Surveys provides "a set of standards for the execution of hydrographic surveys for the collection of data which will primarily be used to compile navigational charts to be used for the safety of surface navigation and the protection of the marine environment." (IHO 2008). The requirements are summarized in S-44 Table 1. The establishment of the various survey order classes (Special Order, Order 1a, Order 1b, and Order 2) are defined by a combination of factors including specific depth ranges, the presence of anthropogenic and/or natural features, and the degree of importance for under-keel clearance. The majority of NOAA surveys fit under the class Order 1a but occasionally Order 1b or Special Order surveys may be required. The minimum standards for the horizontal positioning of topography significant to navigation for an Order 1a or Special Order survey is 2 meters or better at a 95% confidence interval. To be able to accurately determine if a surveyed feature will be bare, awash, or fully submerged at the charted tidal datum, the vertical uncertainties must be held to the same standards as those for soundings: Maximum Allowable Total Vertical Uncertainty (TVU), of 0.25 meters for Special Order, and 0.5 meters for Order 1a and Order 1b.

Feature	Special Order	Order 1a	Order 1b	Order 2
Horizontal positioning of fixed aids to navigation and topography significant to navigation. (95% Confidence level)	2 meters	2 meters	2 meters	5 meters
Positioning of the Coastline and topography less significant to navigation (95% Confidence level)	10 meters	20 meters	20 meters	20 meters
Mean position of floating aids to navigation (95% Confidence level)	10 meters	10 meters	10 meters	20 meters
Maximum Allowable TVU (95% Confidence level)	0.25 meters	0.5 meters	0.5 meters	1.0 meters

Table 3.1: IHO Minimum standards for hydrographic surveys (IHO, 2008)

In this study, the performance of the Velodyne VLP-16 industrial-grade TLS was quantified by evaluating key parameters that are essential for shoreline feature mapping. The results of the performance evaluation were compared to IHO S-44 standards. The system's performance metrics was validated in in a well-controlled environment (laboratory and field) with carefully designed experiments. The laboratory experiments were conducted using the wave and tow tank facilities in the UNH's Jere A. Chase Ocean Engineering Lab. All the field experiments were conducted within Portsmouth Harbor along the Piscataqua River.

Experimental Apparatus

UNH wave and tow tank in Chase Engineering Lab

The UNH wave and tow tank in Chase Engineering Lab is able to simulate the mechanical characteristics of coastal and oceanic waters. The tank is 36.0 m long, 3.7 m wide, and 2.4 m deep. The tank is outfitted with a cable-driven tow carriage that runs on beams that stretch the length of the tank. The tow carriage platform is designed to be a general mounting point for various experimental devices and to accommodate sensors and power sources that feed a data acquisition system. In its present configuration, the carriage is capable of traversing the tank at velocities ranging from 0.1 to 1.5 m/s with a translation accuracy of cm level.

UNH Judd Gregg Marine Research Complex and R/V Gulf Surveyor

UNH also has the Judd Gregg Marine Research Complex that provides UNH faculty and students with access to the open waters of the Gulf of Maine. Located at historic Fort Constitution in New Castle, New Hampshire at the mouth of Portsmouth Harbor. The complex includes a research pier and a floating dock system and is home to several research vessels including the R/V Gulf Surveyor, a 48 foot-long research vessel. The vessel is dedicated to hydrographic and ocean mapping research and is operated primarily in the area of Portsmouth, New Hampshire, but is capable of transiting and operating from Maine to Massachusetts. Although the vessel is designed for offshore operations, it is ideally suited for near-shore and shallow water operations (in as little as four meters of depth). The vessel carries life rafts, an EPIRB (Emergency Position Indicating Radio Beacons), and electronic navigation systems based on GPS, and radar. The vessel offsets from IMU to the TLS were measured using a measuring tape, laser level, and plumb line.

Vessel Name	R/V Gulf Surveyor
Length	48'
Breadth	17'
Draft	4.6'
Positioning and Attitude	Applanix POS-MV
GPS Antennas	(2) Trimble Zephyr
RTK GPS Receiver	Trimble 5700
Acquisition Software	Hypack



Table 3.2: Acquisition vessel, R/V Gulf Surveyor

Alignment

The wave/tow tank functioned as the reference frame control due to the ability to adjust a target with millimeter accuracy along one axis. By holding the position the laser scanner static at the edge of the tank and conducting an alignment procedure, the translation offsets between the two reference frames were well-controlled. In order to monitor the TLS mounting orientation with respect to UNH wave and tow tank, two Thorlabs, Inc. rotating compasses were used: 1) RP01 2-inch Manual Rotation Stage with 1° of resolution and 2) PR01 High Precision Rotating Mount with 0.04° resolution. Both rotating compasses can be coarsely adjusted 360° using the perimeter engravings. The high precision rotation mount can be finely adjusted by fastening a set screw to engage the micrometer. By using the Vernier scale on the micrometer, the compass provides ±5° of fine adjustments at 0.04° increments (THORLABS 2016). The final adjustment for aligning the laser scanner reference frame with respect to a target reference frame, a 1-inch wide (2.5cm)

strip of aluminum was rigidly mounted vertically on a target frame (Figure 3.1 and Figure 3.2). The scanner/target pair was aligned in two steps. First, the vertical alignment was accomplished by translating the height of the reported optical center of the scanner to the physical center of the target. Then, the horizontal alignment was accomplished by intersecting the $+1^\circ$ beam with the vertically narrow target at various ranges. Because the scanner's 16 laser beams are divided into a $\pm 15^\circ$ FOV with typically a 2° separation between the laser beams, it was not possible to align the TLS at the center (i.e., 0°). Instead, the TLS was aligned at 1° off-center with respect to the laser scanner reference frame. Real-time data from the TLS measurements were queried using the Velodyne native visualization software, Veloview. Rotational alignment was achieved by slowly rotating the target back and forth until the maximum intensity was achieved. The maximum intensity measurement was interpreted as the laser scanner being orthogonal to the aluminum strip based on the assumption that the peak return to the TLS is at a nadir incident angle of the laser beam to the target. To achieve translational alignment, the real-time horizontal coordinates of the laser measurements at various ranges from the target were compared to geometric calculations of laser measures in a perfect alignment configuration. If these values differed, manual adjustment of the laser scanner's across-track position was performed. The rotational and translational alignment procedures were conducted iteratively until the scanner/target pair were well-aligned. Once aligned, laser measurement data was collected using VeloView in the proprietary format, .pcap, exported to .csv, and processed in MATLAB.

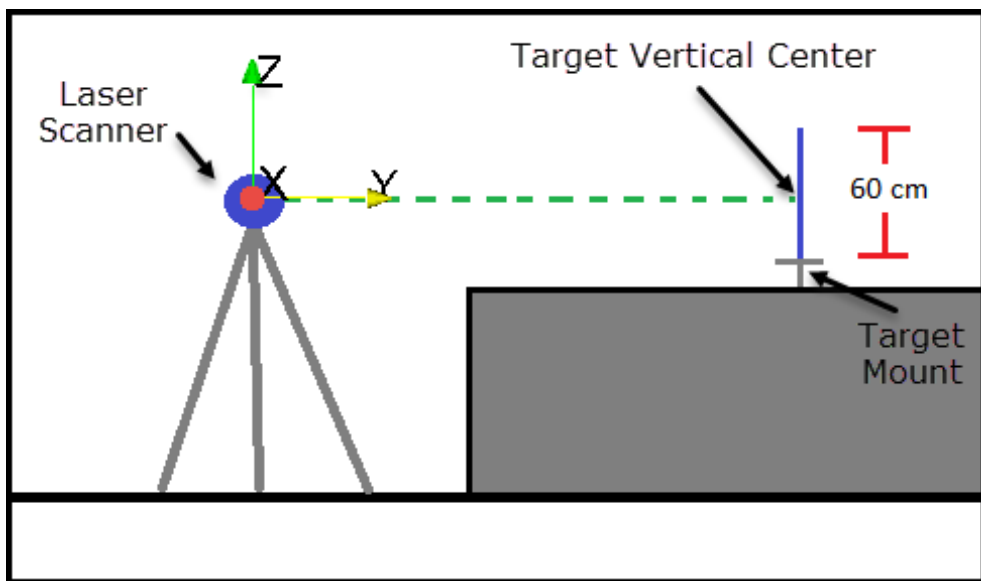


Figure 3.1: Illustration of experiment set-up with laser scanner's reference frame (side view).

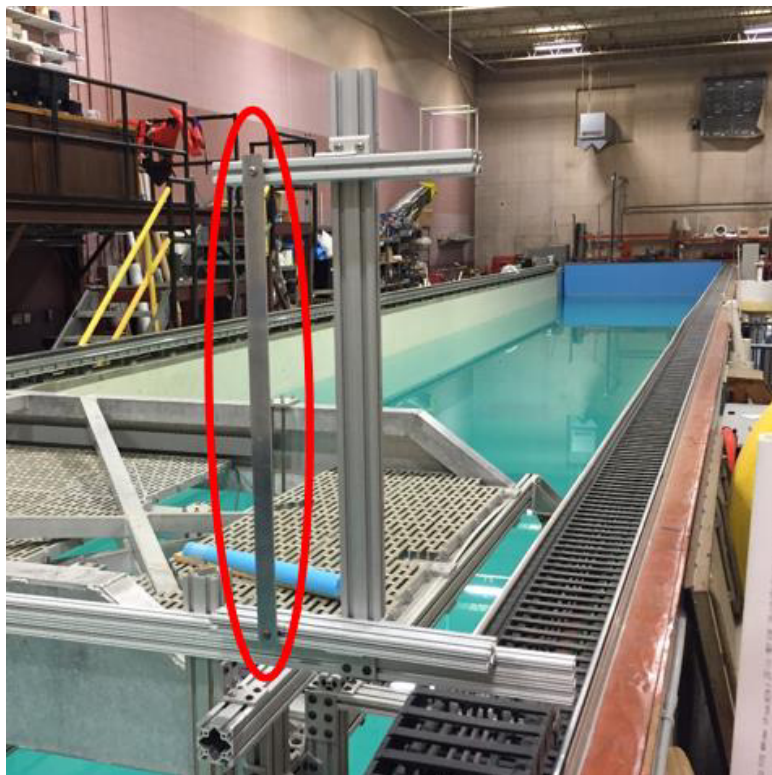


Figure 3.2: A 1-inch wide strip of aluminum used as an alignment target. The strip is vertically mounted to a rigid frame.

Laser Beam Orientation

The purpose of this experiment is to independently assess the VLP-16 laser scanner's reported beam orientation. The 16 laser beams of the TLS are reported to be distributed evenly within a FOV of $\pm 15^\circ$ of elevation angles (Velodyne Lidar, 2015), resulting in 2° separation between each beam (Table 2.2). In survey mode, the scanner rotates 360° (in azimuth) along a vertical axis. For each point, XYZ positions with respect to the laser reference frame are obtained by converting from the spherical coordinates to Cartesian coordinates as follows where α is the azimuth angle, β is the elevation angle, and R is the range:

$$\text{Equation 3.1: } x = R * \cos(\beta) * \sin(\alpha)$$

$$\text{Equation 3.2: } y = R * \cos(\beta) * \cos(\alpha)$$

$$\text{Equation 3.3: } z = R * \sin(\beta)$$

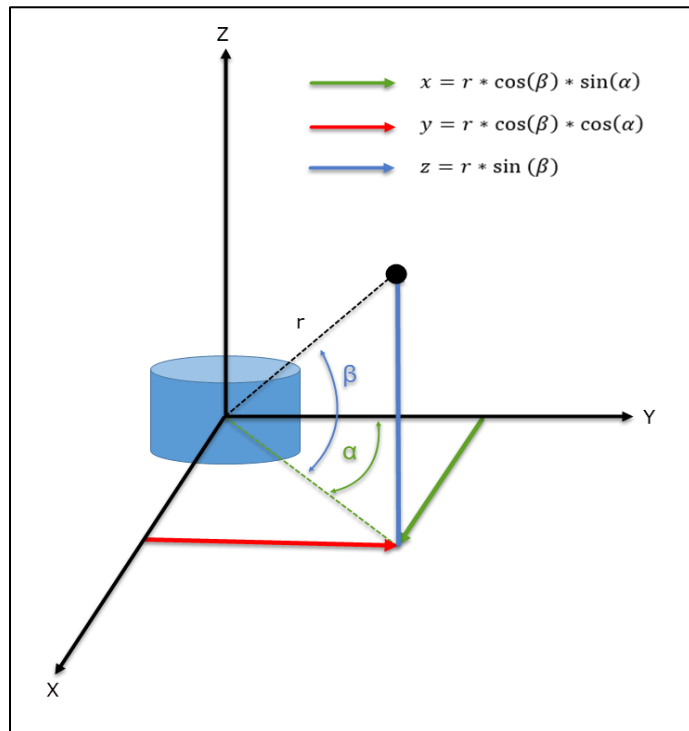


Figure 3.3: Conversion from spherical coordinates to Cartesian coordinates.

Measurement of the angular separation between laser beams was achieved by identifying the peak intensity value of laser measurements that intersect a vertical specular target (aluminum strip) using a high precision rotating compass. The average intensity within the specular area of the target was computed for each setup. The relative angular separation between laser beams was identified by finding at what precise angles the peak intensity occurred for each beam. Additionally, the uncertainty of the angular separation was computed by calculating the variation of β angles for each data point within the specular area of the target and calculating the 2σ confidence interval for each laser beam.

The laser scanner was mounted to scan vertically above the high precision horizontal rotating compass by using a custom fabricated 90° aluminum angle bracket (Figure 3.4). The fastener holes and set-pins of the custom angle bracket were positioned such that the reported optical center of the scanner was centered above the rotating platform's vertical axis of rotation. The laser scanner and rotating platform unit were then mounted above a level tripod which was positioned at the edge of the tow tank.

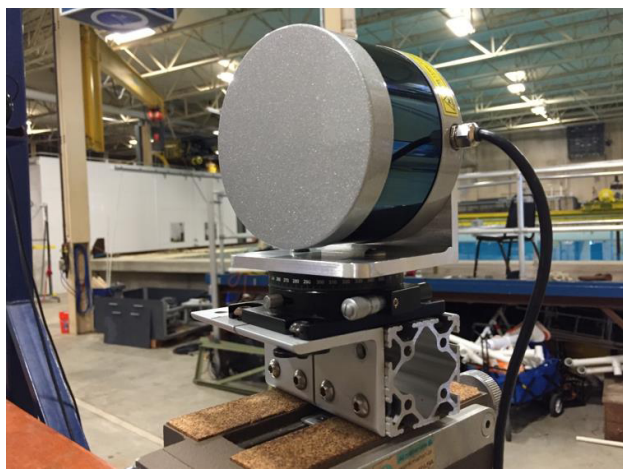


Figure 3.4: VLP-16 laser scanner mounted above a high precision rotating compass.

Because the high-resolution compass could only be adjusted within a range of $\pm 5^\circ$ due to the limited range of the micrometer, four sets of measurements were established on the -11° , -3° , $+3^\circ$, and $+11^\circ$ laser beams to cover the full range of the scanner ($\pm 15^\circ$), as shown in Figure 3.5. From each of these relative reference frames, the angular offsets of the surrounding four laser beams were measured in 20 setups, resulting in redundant measurement between the -7° , -1° , $+1^\circ$, and $+7^\circ$ beams. The high precision angular offsets between each beam were measured by rotating the scanner by small intervals of 0.04° around a $\pm 0.24^\circ$ window surrounding a particular laser beam. This resulted in 13 measurements per setup, shown in Figure 3.6. Data were collected for 20 seconds at each 260 setup configurations (4 reference frames x 5 lasers per reference frame x 13 measurements per laser).

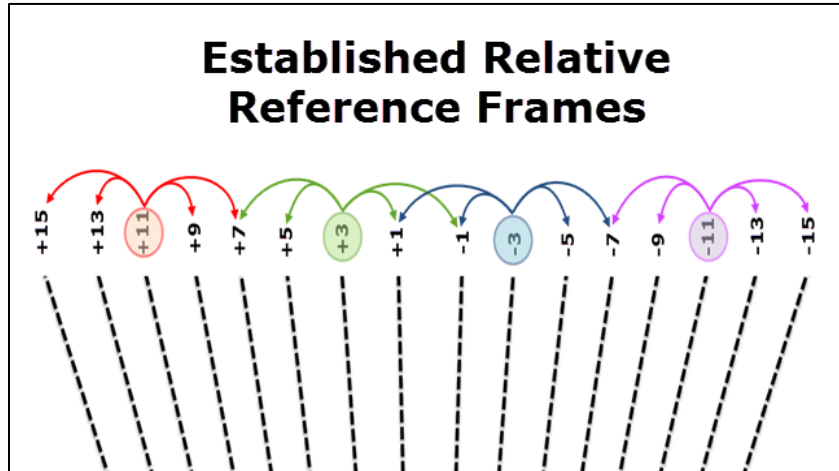


Figure 3.5: Relative reference frames were established on the -11° , -3° , $+3^\circ$, and $+11^\circ$ beams to cover the $\pm 15^\circ$ window of the scanner. From each of these reference frames, the four surrounding laser beams were verified.

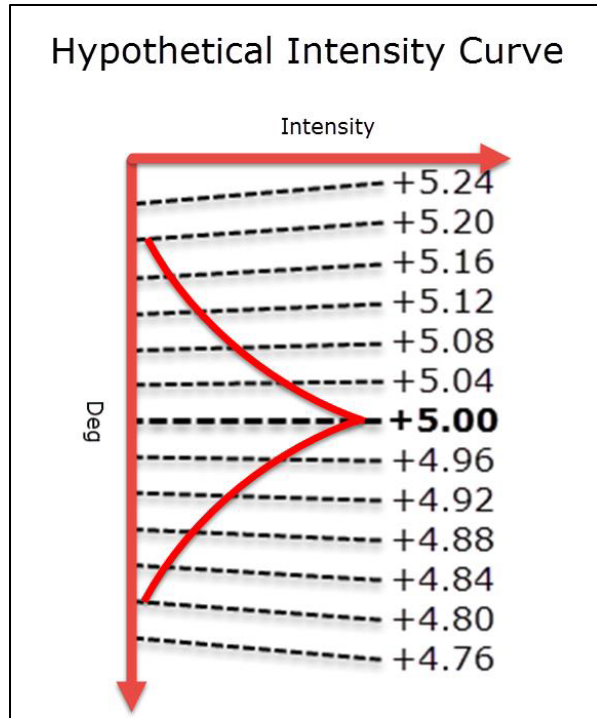


Figure 3.6: Hypothetical intensity returns, centered around the $+5^{\circ}$ beam, from rotating the scanner by increments of 0.04° through a window of $\pm 0.24^{\circ}$ centered on the assumed location of the laser beam.

Estimating Range Uncertainty

The purpose of this experiment was to independently assess the VLP-16 laser scanner's ranging performance on various targets at discrete ranges and incident angles. Target materials were selected with surface characteristics similar to features that would commonly be found in a port or harbor setting. From smoothest to roughest, the targets selected were whiteboard (analogous to a freshly painted boat or a metal buoy), wood (analogous to a wooden pier or piling), concrete (analogous to a weathered rock or concrete pier), and sand (analogous to a sand or pebble beach) shown in Figure 3.7. In addition, the intensity values of the range measurements were also evaluated. Figure 3.8 shows a point cloud which depicts the experiment setup with the laser scanner at the edge of the tow tank and the target mounted on the tow carriage.



Figure 3.7: Four targets used for estimating ranger uncertainty. From left to right; whiteboard, wood, concrete, and sand.

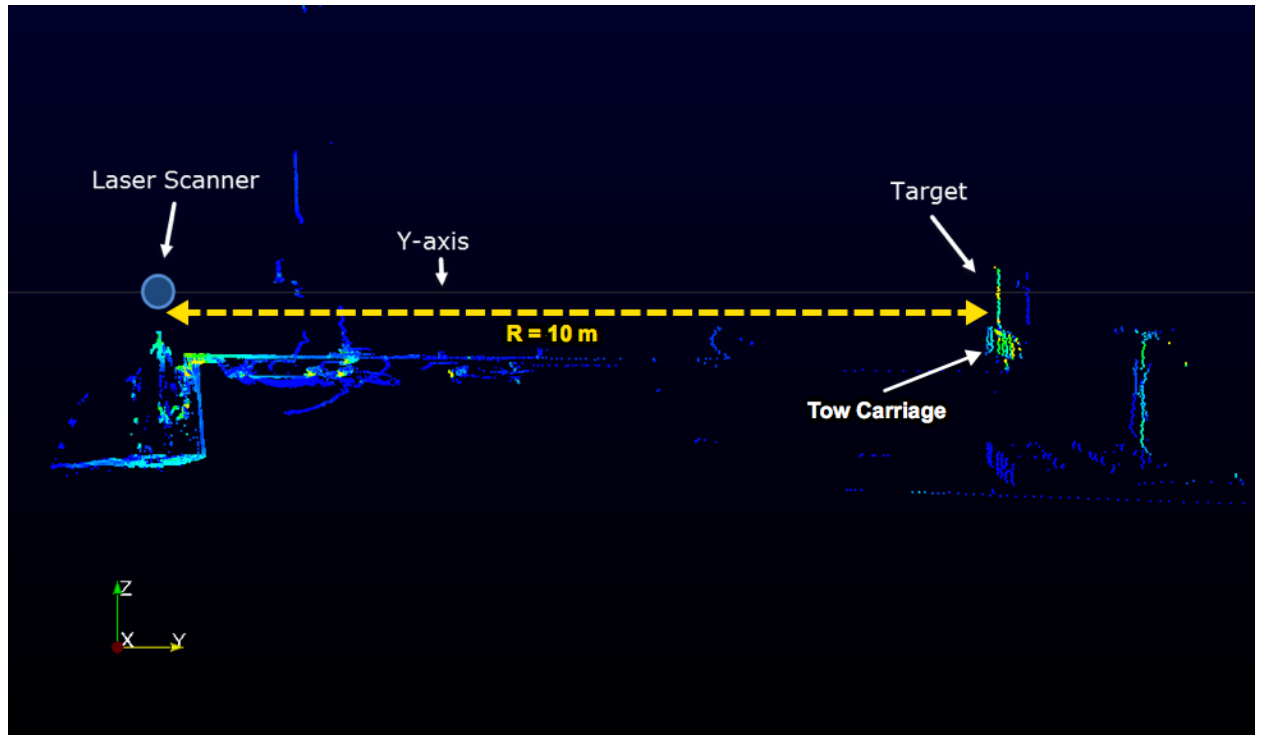


Figure 3.8: Experiment setup with laser scanner setup vertically on tripod at edge of the tow tank and the target mounted to the tow carriage at 10 m range.

Next, the data was clipped so that only the near-nadir returns were considered, specifically within a bin size of ± 5 cm from the center of the specular area. This was accomplished by calculating an azimuth window for each range and filtering out data outside of that window shown in Figure 3.9. The data were then centered on the origin of the TLS reference frame by subtracting the average range of the measurements on the target for each range in the normal incident angle configuration. Data were then binned into 2.5 cm vertical bins and statistics (mean and standard deviation) were calculated for each setup configuration including the 2σ confidence interval (CI).

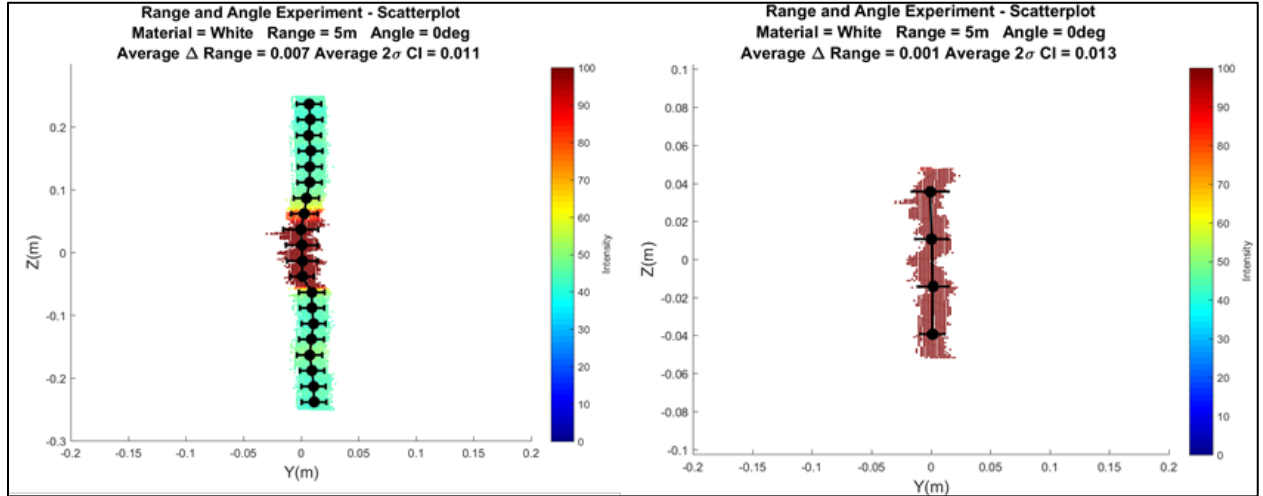


Figure 3.9: Clipped data resulting from an azimuth window filter. Left- before filtering. Right- after filtering.

Data Density

In order to evaluate the amount of point measurements per area that can be expected on a target along the shoreline using a single survey line, a geometrical computer simulator was created to generate a theoretical dataset. For comparison, the same scanner configurations were used in a

field performance evaluation on a marine survey vessel. The PRR for the VLP-16 is advertised to be up to 300,000 points per second.

The computer simulator was created in the MATLAB environment and was a geometric simulation that evaluated the intersection of the laser beams on a vertically flat target at any range. The mechanical characteristics of the VLP-16 laser scanner used in the simulations included the number laser channels, beam separation, pulse repetition rates, and scanner rotation rates. By providing a specific vessel speed, distance, and orientation with respect to the target, it is possible to evaluate the data density within a 1m^2 window (Figure 3.10). It should be noted that this simulator is modular and can be modified to evaluate other mechanical scanners of interest. Additionally, random vessel rotations (roll, pitch, yaw) can be introduced to the simulations to evaluate the effects of vessel motion due to wave action in realistic environmental conditions.

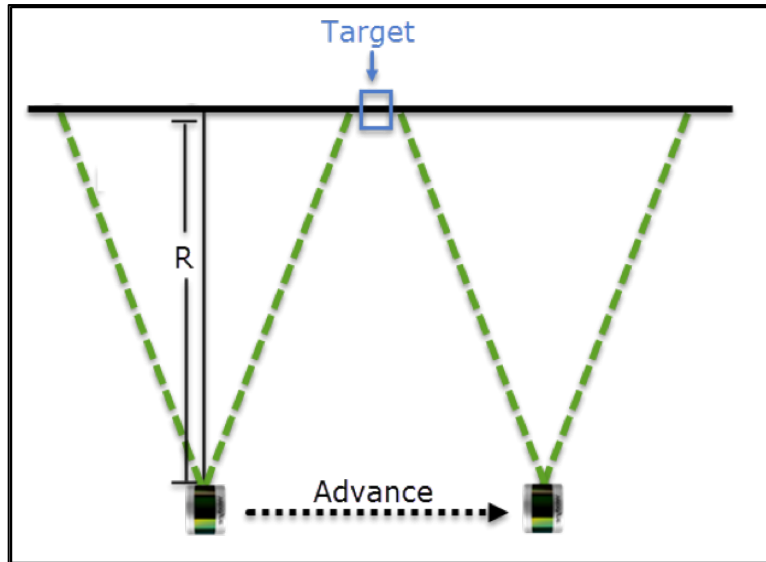


Figure 3.10: Top down view of geometric computer simulation where R is the range from the scanner to the planar target.

Simulations were conducted at ranges 10-100 m at 10 m increments. The scanner system was configured at rotation rates of 5 Hz and 20 Hz, and in two mounting configurations, vertically and with a 45° pitch angle forward. These various configurations resulted in 40 lines of data (10 ranges x 2 rotation rates x 2 mounting orientations). The scanner speed of advance was 4 kt.

For comparison, a field performance evaluation dataset was collected on 19 October, 2016 aboard the R/V *Gulf Surveyor* (RVGS) within Portsmouth Harbor along the University of New Hampshire pier at the Judd Gregg Marine Research Complex. One of the vertical flat concrete surfaces of the pier was used as a target. The flat area is located between the first two bollards near the end of the pier (Figure 3.11). This target was selected because of the physical surface characteristics and survey logistics, the surface is considered very smooth and it is possible to scan the target from a survey vessel at distances greater than 100 m. After the TLS system was mounted and aligned on R/V Gulf Surveyor, measurements of the vertical target were collected along survey lines parallel to the UNH pier-face in configurations which mimicked the computer simulations: at ranges 10-100 m at 10 m increments, scanner rotation rates of 5 Hz and 20 Hz, and in two mounting configurations, vertically and with a 45° pitch angle forward. The direction of the survey lines were northeast to southwest. Again, these various configurations resulted in 40 lines of data (10 ranges x 2 rotation rates x 2 mounting orientations). All lines of data were acquired with the intent of maintaining a speed over ground of 4kt and minimizing changes of heading.

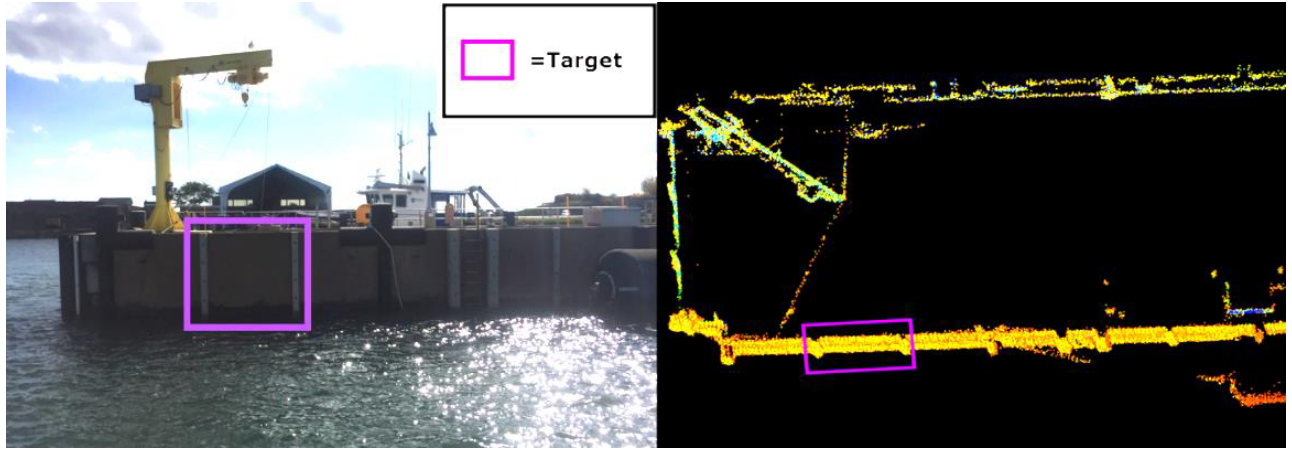


Figure 3.11: Target for the data density experiment was a vertical flat and relatively smooth area of the UNH pier-face. Left: A side view of the pier-face. Right: Top-down view of data on pier-face from one pass.

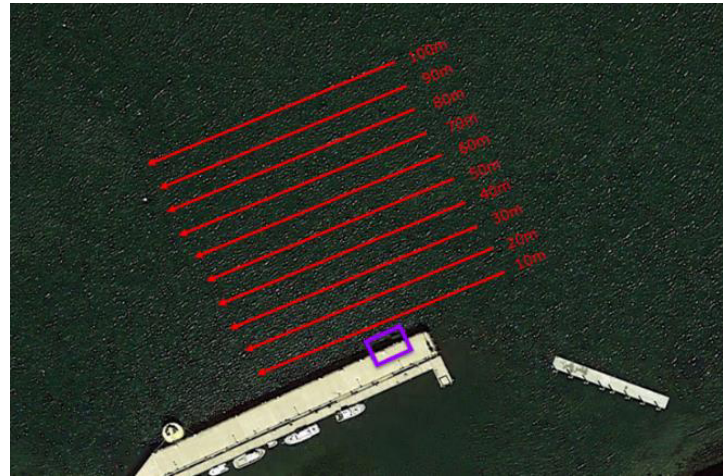


Figure 3.12: Northeast to southwest lines from 10-100 m. Purple box is the target of interest. Not drawn to scale.

Data processing was completed in MATLAB. First, the data was manually cleaned to remove flyers and cropped so that the only points that remained were on the target. A center point was identified by averaging the X, Y, Z geographic coordinates of a dense point cloud at a range of 10 m to identify the center of the target. This coordinate was then used as the center point for all

remaining lines. A 1 m^2 window was then generated at the center point and aligned with the vertical surface. Alignment was achieved by using the MATLAB function ‘affine fit’, which calculates best fit of the point cloud to a plane using least squares approximation. The plane and the associated points were then re-projected into the TLS reference frame according to the reported orientation of the system.

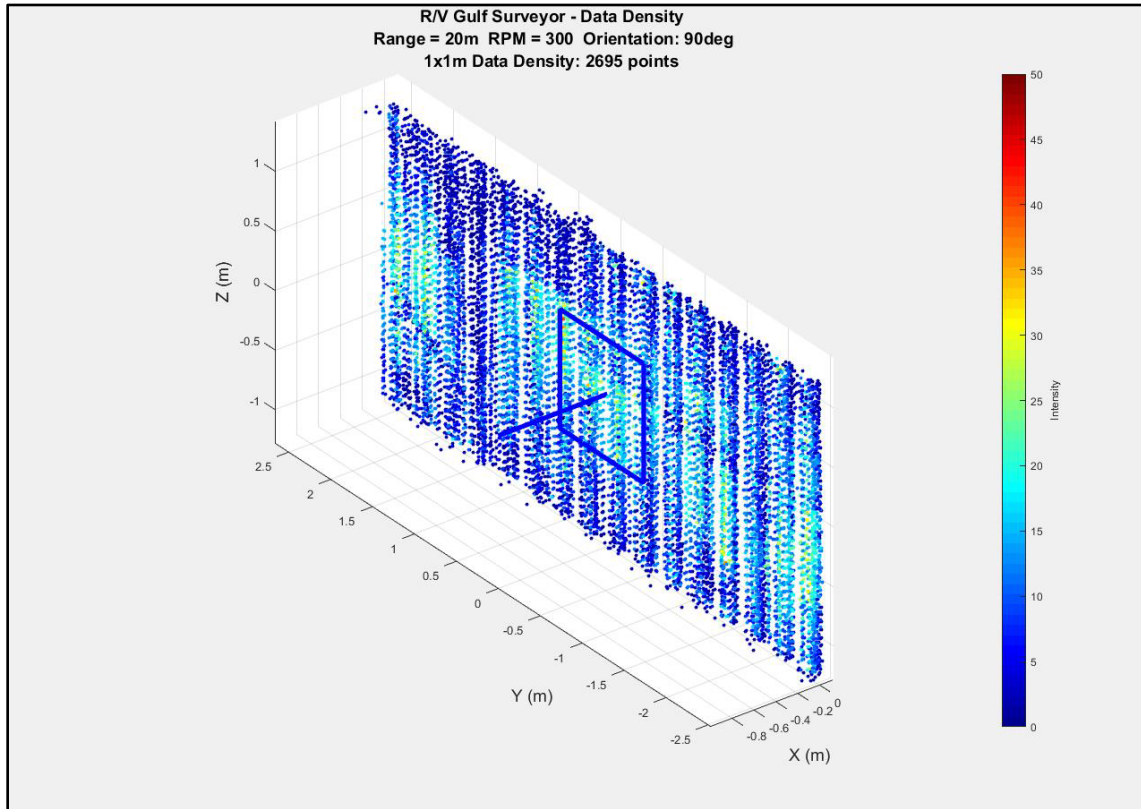


Figure 3.13: Example of data density within a 1 m^2 box, normal vector shown.

4. Results

Laboratory experiments and field work were conducted in order to evaluate the performance of the Velodyne VLP-16 laser scanner for mapping surface features and its ability to interface with a vessel's auxiliary global navigation satellite system (GNSS) and inertial navigation system (INS) by using HYPACK's HYSWEEP module. The goals of the study were: 1) an independent assessment of the laser scanner's performance in estimating range, accuracy, data density, and the ability to detect various target materials in a well-controlled environment and 2) an evaluation of different survey configurations for detecting and characterizing surface features in field work. The work conducted in this study provided an independent assessment of the laser scanner's performance that included: 1) laser beam orientation, 2) range, and 3) data density.

Experiments were performed in the Jere A. Chase Ocean Engineering Laboratory at the University of New Hampshire under controlled settings to characterize each of the laser scanner's performance parameters. Field work was conducted using the R/V Gulf Surveyor around Portsmouth Harbor, NH to validate the performance parameters and to evaluate various survey configurations.

Laser Beam Orientation

The mechanical calibration of the Velodyne VLP-16 as part of the internal reference frame validation was conducted on the wave and tow tank by using a high-precision rotating compass. The 2° angular separation between neighboring beams (according to the published specifications) for the Velodyne VLP-16 laser scanner was investigated in well-controlled laboratory conditions.

The TLS was mounted in a vertical scanning orientation on top of a high-precision rotating compass with a 0.04° resolution. A target (2.5 cm aluminum strip) was placed at about 8 m distance from scanner. The angular separation with respect to each beam was measured by rotating the compass by small intervals so that each laser beam intersected the target. The scanner-target pair was considered to be in perfect alignment when the peak intensity of the data within the specular area of the target was observed at a given scanning angle, which was interpreted as the entire laser beam footprint was on the target. Because the rotating compass could only be adjusted with high-precision within a 10° range at a time (i.e., $\pm 5^\circ$ from the center of the reference frame), 4 overlapping reference frames were used to provide a full $\pm 15^\circ$ scanning range (Figure 3.5).

It should be noted that when adjusting the micrometer on the rotating compass, a $\sim 0.08^\circ$ of mechanical measurement error was determined by the following actions: The real-time peak intensity was found for a particular beam by rotating the micrometer clockwise (right-handed treads). The micrometer was then set to zero by unscrewing the coarse set-screw, placing the micrometer on zero, and then tightening the set-screw again. If the micrometer was rotated counterclockwise and then rotated clockwise again to the original zero, it is assumed that the location of the laser beam would be oriented to the same location (i.e., the same peak intensity was registered). If TLS is not positioned at the same exact orientation, the intensity values of the laser measurements between the two TLS configurations will differ, i.e., a value less than peak intensity will be measured in the second configuration. By orienting the TLS counterclockwise an additional 0.08° , the peak intensity was again identified. With this finding, care was taken throughout the experiment to always approach the desired angular configuration by rotating the

micrometer in the same direction (always clockwise). Results from the mechanical calibration are presented below in Figure 4.1, Figure 4.2, Figure 4.3, and Figure 4.4.

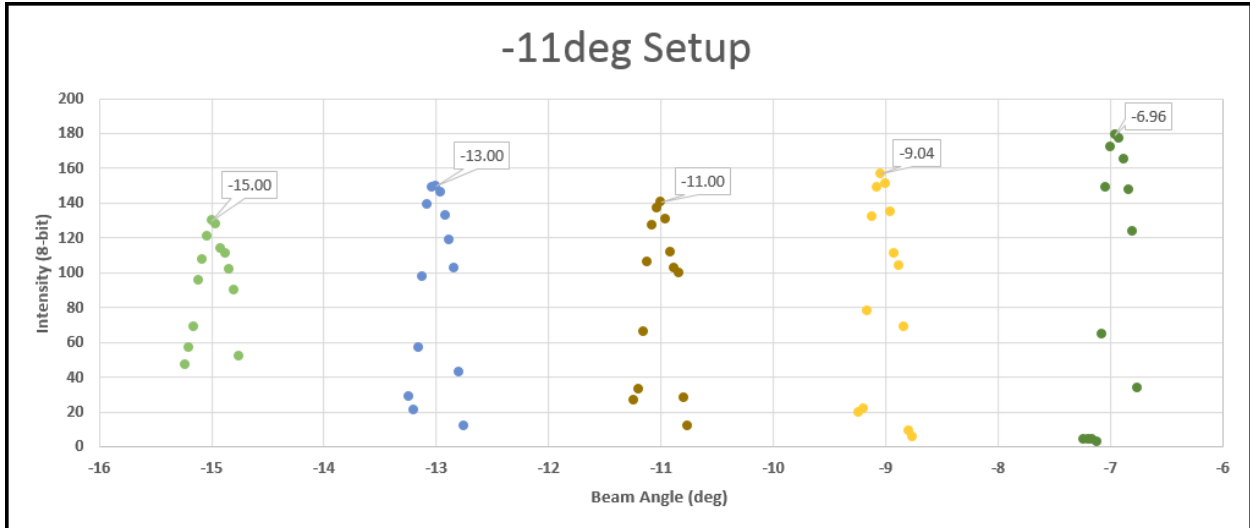


Figure 4.1: Angular separation measured with respect to the four neighboring beams with a reference frame established on the -11° beam.

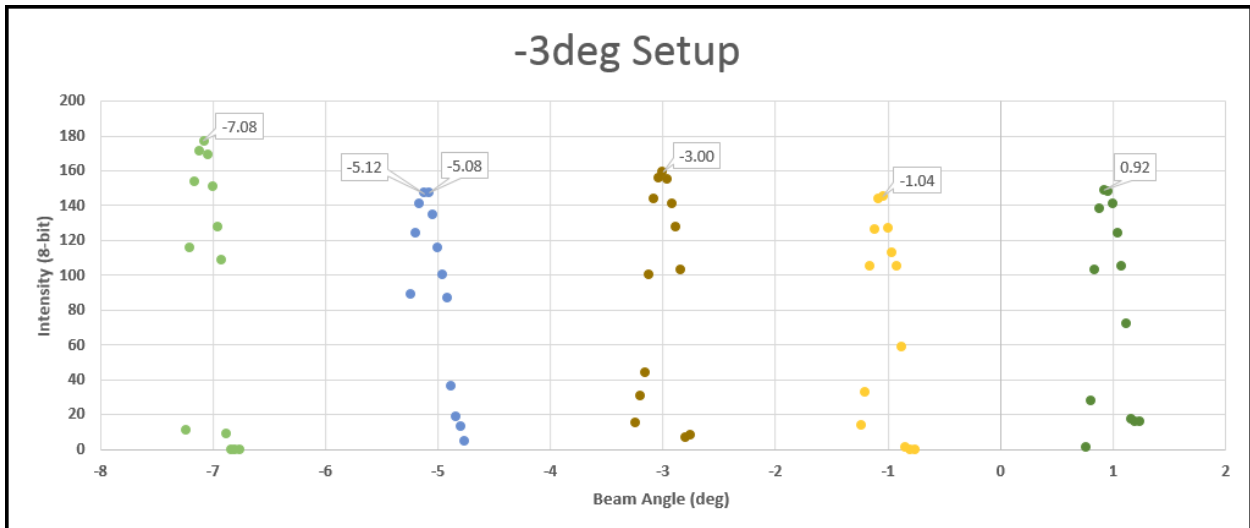


Figure 4.2: Angular separation measured with respect to the four neighboring beams with a reference frame established on the -3° beam.

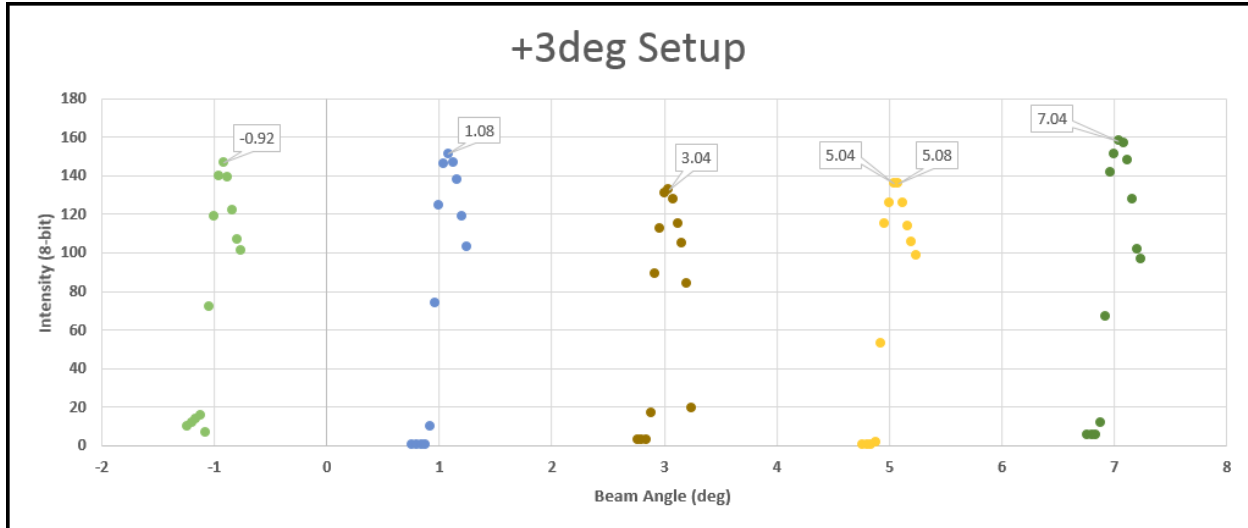


Figure 4.3: Angular separation measured with respect to the four neighboring beams with a reference frame established on the $+3^\circ$ beam.

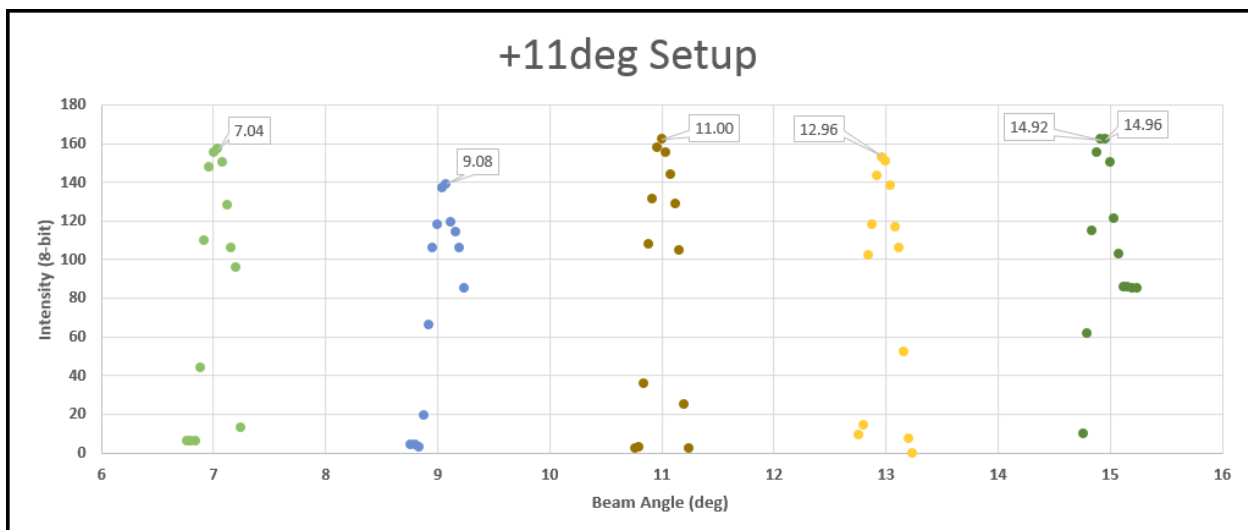


Figure 4.4: Angular separation measured with respect to the four neighboring beams with a reference frame established on the $+11^\circ$ beam.

The mean and standard deviation of the angular separation were compiled from the results (Table 4.1). In order to display all the results over the full $\pm 15^\circ$ scanning range (Figure 4.5), a master reference frame was established on the -11° beam and used as a control for the other three

reference frames. It is important to note that between the reference frames established on the -3° and $+3^\circ$ beams did not overlap perfectly with a -0.04° resolution (Table 4.1), which is the maximum resolution and measurement accuracy of the rotating compass.

Published Angle	Relative to -11		Relative to -3		Relative to +3		Relative to +11		Averaged Δ
	Measured	Δ	Measured	Δ	Measured	Δ	Measured	Δ	
+15							14.94	-0.06	-0.06
+13							12.96	-0.04	-0.04
+11							11	0	0
+9							9.08	0.08	0.08
+7					7.04	0.04	7.04	0.04	0.04
+5					5.06	0.06			0.06
+3					3.04	0.04			0.04
+1			-0.92	0.08	1.08	0.08			0.08
-1			-1.04	-0.04	-0.92	0.08			0.02
-3			-3	0					0
-5			-5.1	-0.1					-0.1
-7	-6.96	0.04	-7.08	-0.08					-0.02
-9	-9.04	-0.04							-0.04
-11	-11	0							0
-13	-13	0							0
-15	-15	0							0

Table 4.1: Measured offsets from mechanical calibration and deviations from expected angle.

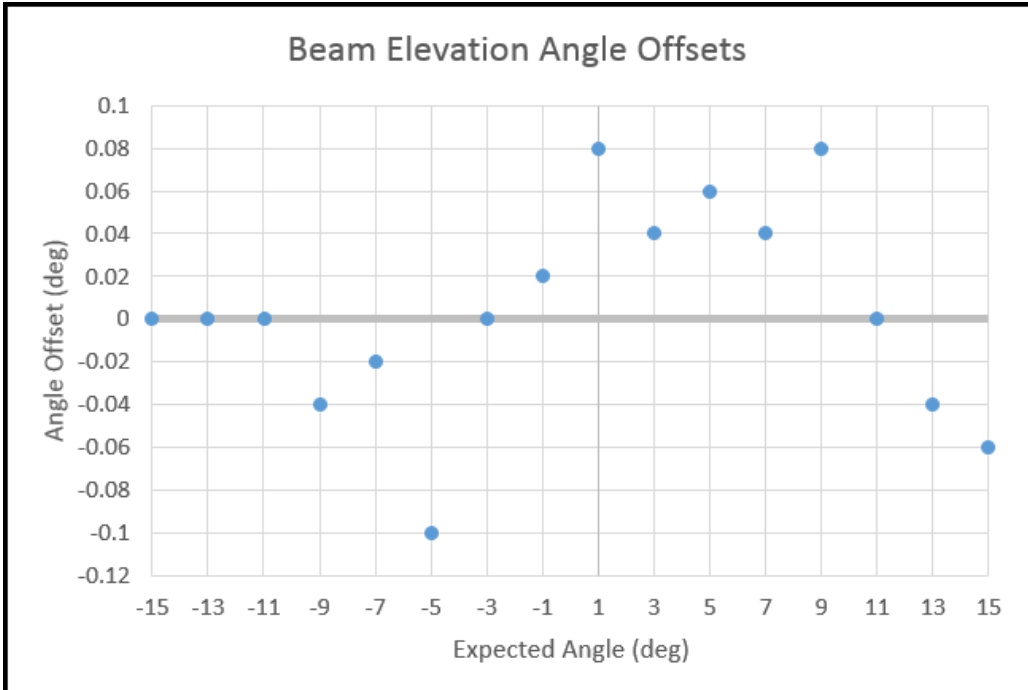


Figure 4.5: Scatterplot of deviations from expected angle for each beam.

The elevation angle uncertainty for each beam was characterized by looking at the variation of the z-coordinate using Equation 3.3 (i.e., conversion from spherical coordinates to Cartesian coordinates). The data from the internal reference frame validation were used to estimate the variation of the β angles. It is important to note that the average range to the target, R , did not change during the experiment, and the z values for all the laser measurements were within the ± 5 cm of the peak value area of the target. The variation of the results for each beam were on average 0.06° at a 2σ confidence interval (Table 4.2).

Laser Angle	15°	13°	11°	9°	7	5	3	1
Angular 2σ								
CI	0.062	0.062	0.064	0.062	0.060	0.062	0.063	0.064
Laser Angle	-1°	-3°	-5°	-7°	-9°	-11°	-13°	-15°
Angular 2σ								
CI	0.063	0.066	0.062	0.064	0.061	0.064	0.061	0.061

Table 4.2: Elevation angular uncertainty at 2 σ CI

Estimating Range Uncertainty

After characterizing the angular separation, range uncertainty of the Velodyne VLP-16 was characterized. Three key parameters that were evaluated included: distance from the scanner, orientation of the target with respect to the incident laser beam, and reflection characteristics of the target. The scanner was held static throughout the experiment on a leveled tripod at the edge of the tow tank. Different targets with various surficial roughness (i.e., whiteboard, wood, concrete, and sand) were mounted above a rotating compass at different ranges and incident angles from the laser scanner. Range results only within a ± 5 cm of the peak value area of the target are shown from a side-view in Figure 4.6 - Figure 4.9, where the laser scanner is to the left of each plot. For each target, there is a clear inverse relationship between the incident angle of and intensity of the laser measurement. A possible explanation is that most of the laser light is being foreshattered and less laser light being backscattered to the laser scanner's detector at large incident angles. This effect is most pronounced for the smoothest target and least pronounced for the roughest target due to its faceted surface.

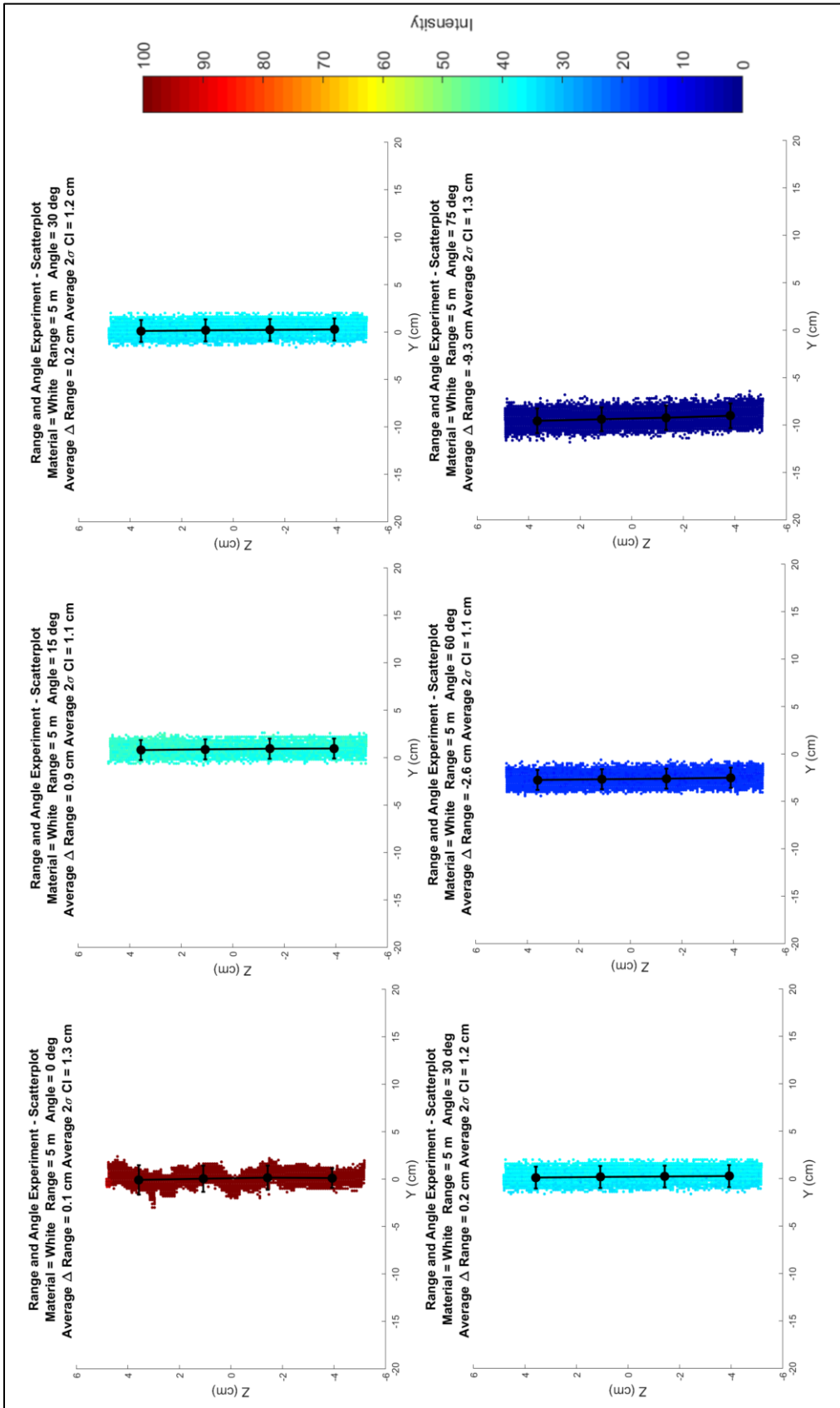


Figure 4.6: Range measurements to a whiteboard target at various incident angles, where data points are colored by intensity and four black horizontal error bars represent the 2σ CI for each 2.5cm vertical bins.

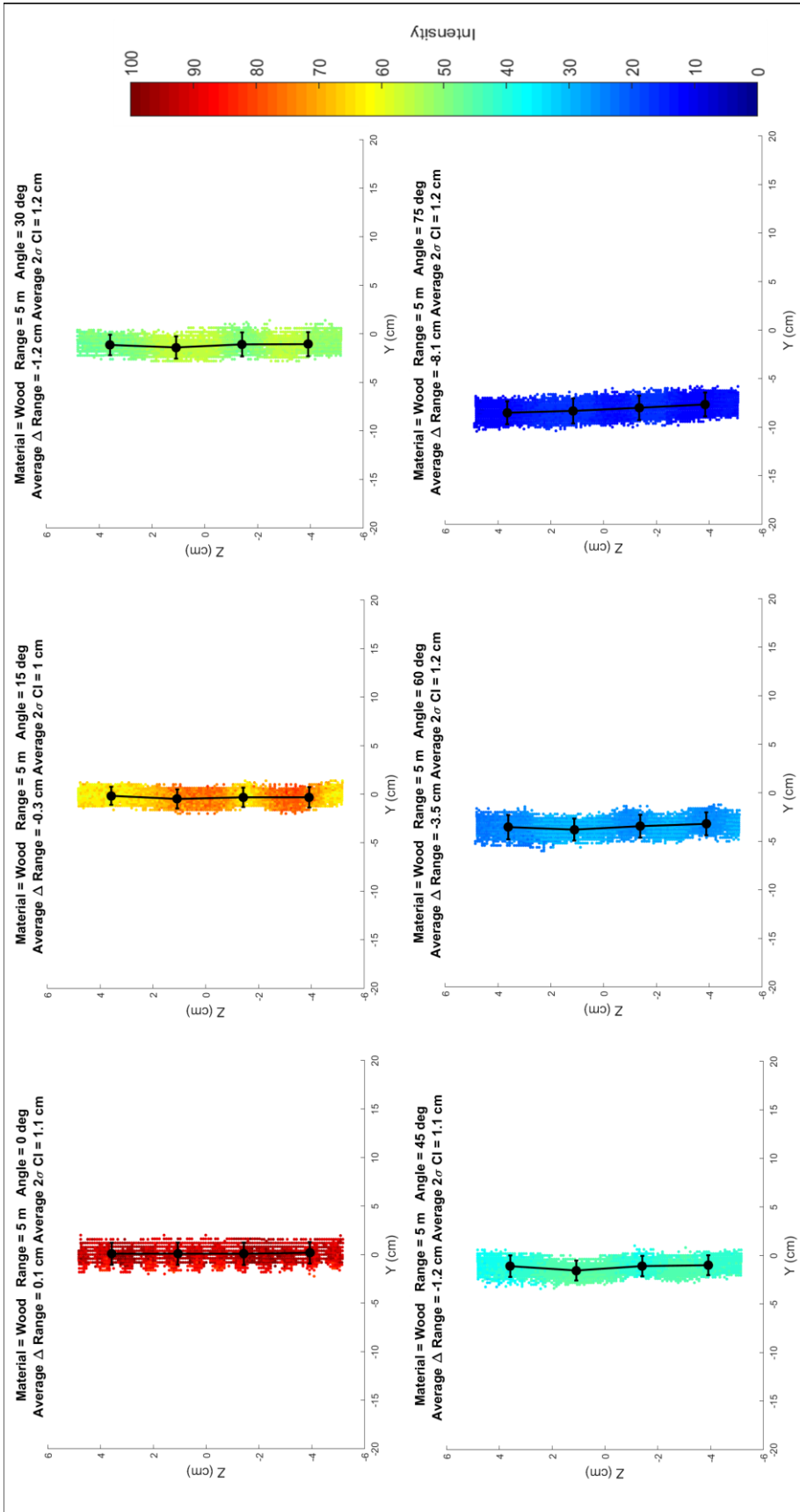


Figure 4.7: Range measurements to a wood target at various incident angles, where data points are colored by intensity and four black horizontal error bars represent the 2σ CI for each 2.5cm vertical bins.

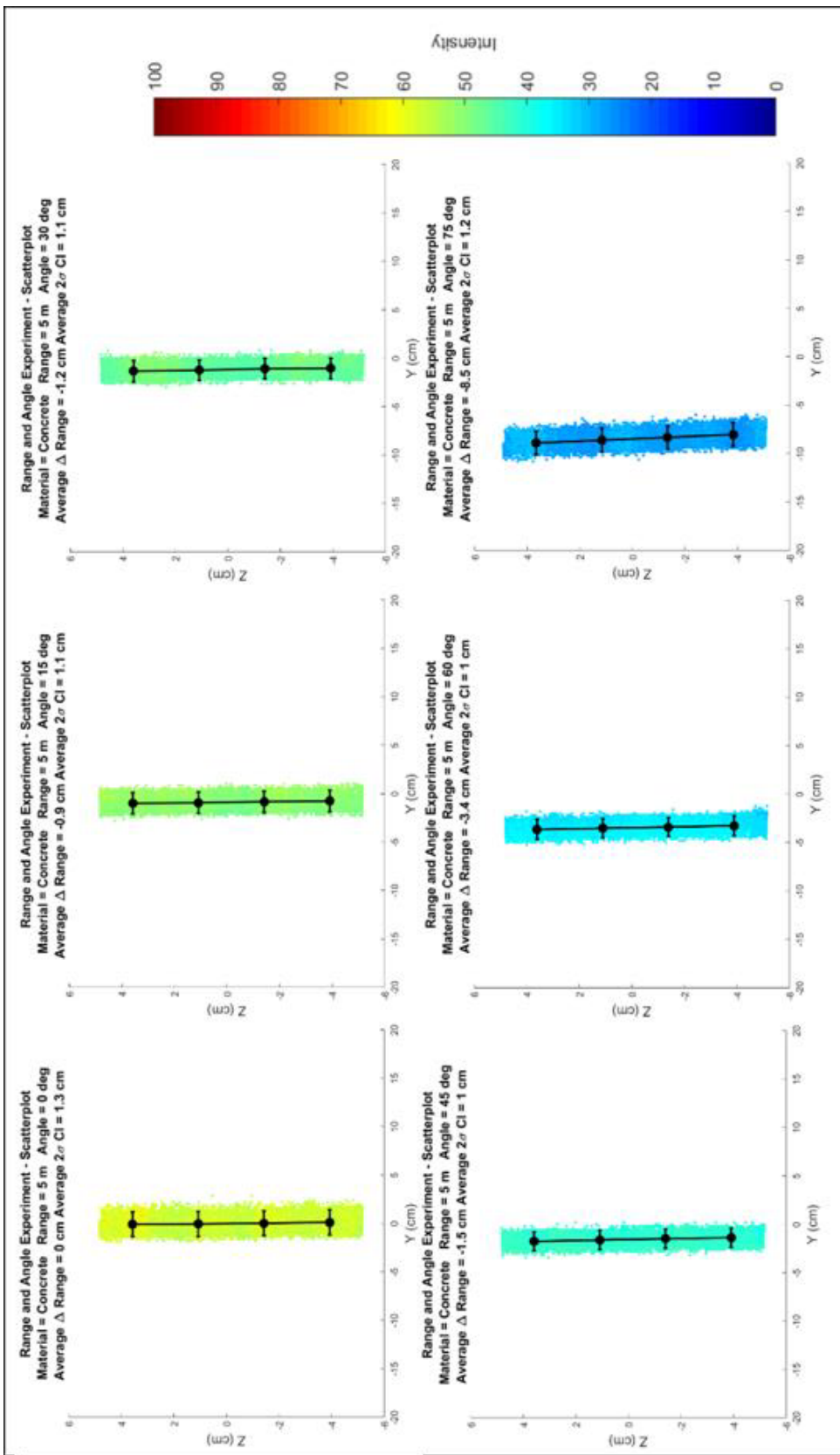


Figure 4.8: Range measurements to a concrete target at various incident angles, where data points are colored by intensity and four black horizontal error bars represent the 2σ CI for each 2.5 cm vertical bins.

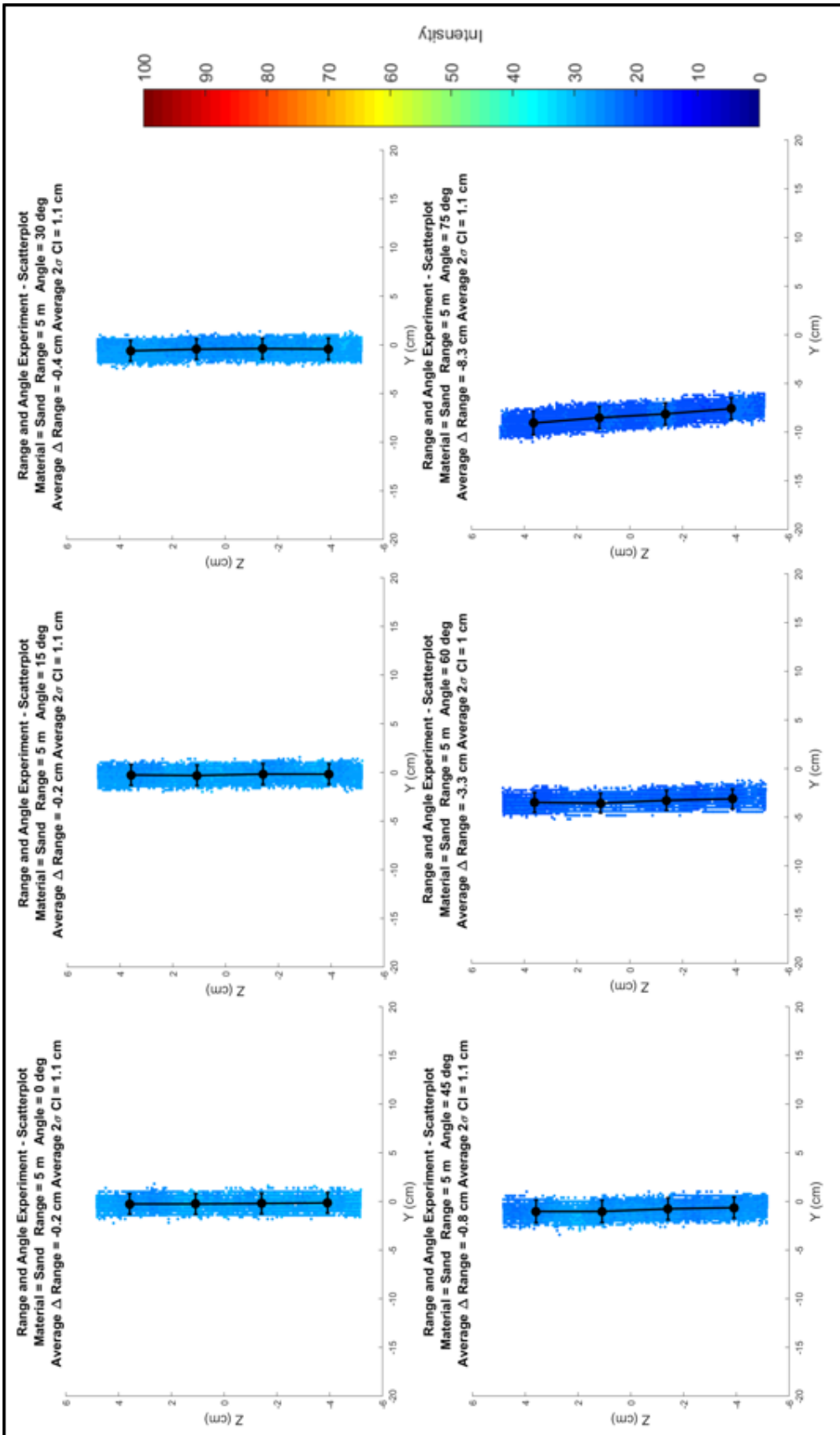


Figure 4.9: Range measurements to a sand target at various incident angles, where data points are colored by intensity and four black horizontal error bars represent the 2σ CI for each 2.5cm vertical bins.

In addition to the intensity, it seems that there is also an inverse relationship with range from the scanner to the target and incident angle. A possible explanation to the range offset at large incident angles is the geometric characteristics of the laser beam footprint intersecting with the target's leading edge as it is rotated (Figure 4.10). It is possible that the first photons returning to the laser scanner's detectors are from the leading edge causing a detection. This issue is common with LiDAR systems that do not collect the full waveforms (Maune, 2007).

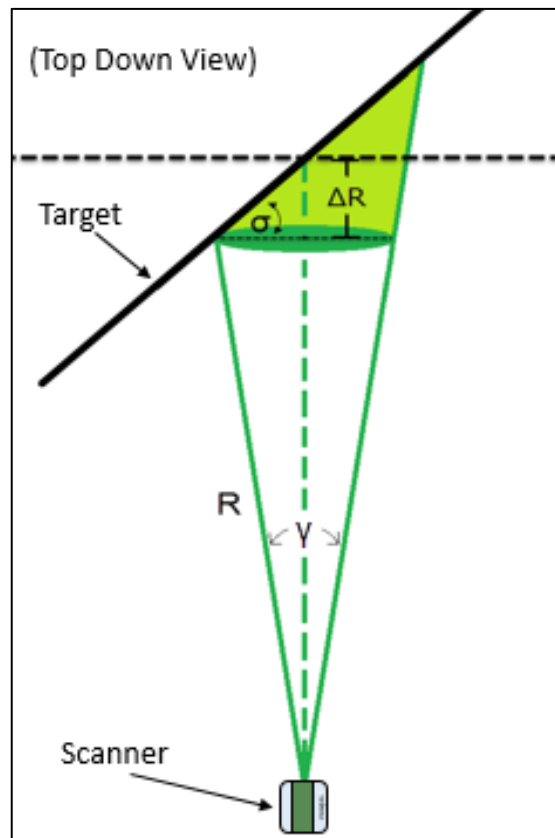


Figure 4.10: Oblique target and intersecting laser beam footprint.

The range uncertainty of the VLP-16 laser scanner measurements was calculated using the four 2.5 cm vertical bins over the specular area of the target, covering an area of ± 5 cm from the center. For each bin, the 2σ CI of the raw range estimates was calculated. Finally, the four bins were averaged together for each setup. Figure 4.11 shows these averaged 2σ CI for each target at all ranges and incident angle configurations.

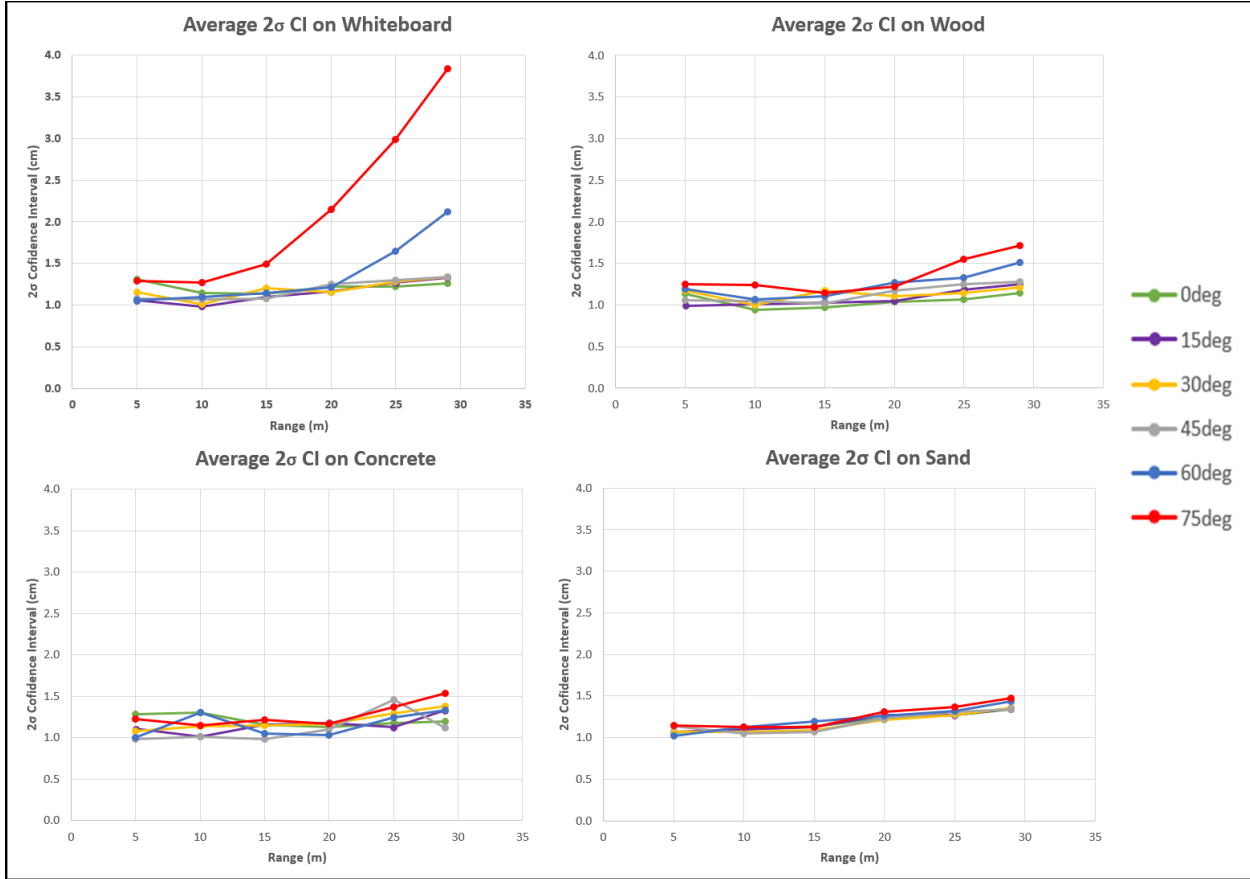


Figure 4.11: Average 2σ CI for all targets.

There is a strong inverse relationship between surficial roughness and 2σ CI at large incident angles. The scanner performed well in all conditions for the faceted sand target and performed poorly on the specular surface of the whiteboard target at large incident angles. The average 2σ CI for all targets at all incident angles at the maximum range of 29 m was 1.5 cm. Due to the

physical limitation of the size of the tow tank, it was not possible to assess the TLS range uncertainty at its maximum range of 100 m. Second power polynomial trend lines for each curve in Figure 4.11 were calculated and extrapolated out to 100 m shown in Figure 4.12. In most range and incident angle configurations, especially at large incident angles, the 2σ CI at 100 m range were above the advertised accuracies of 3.0 cm.

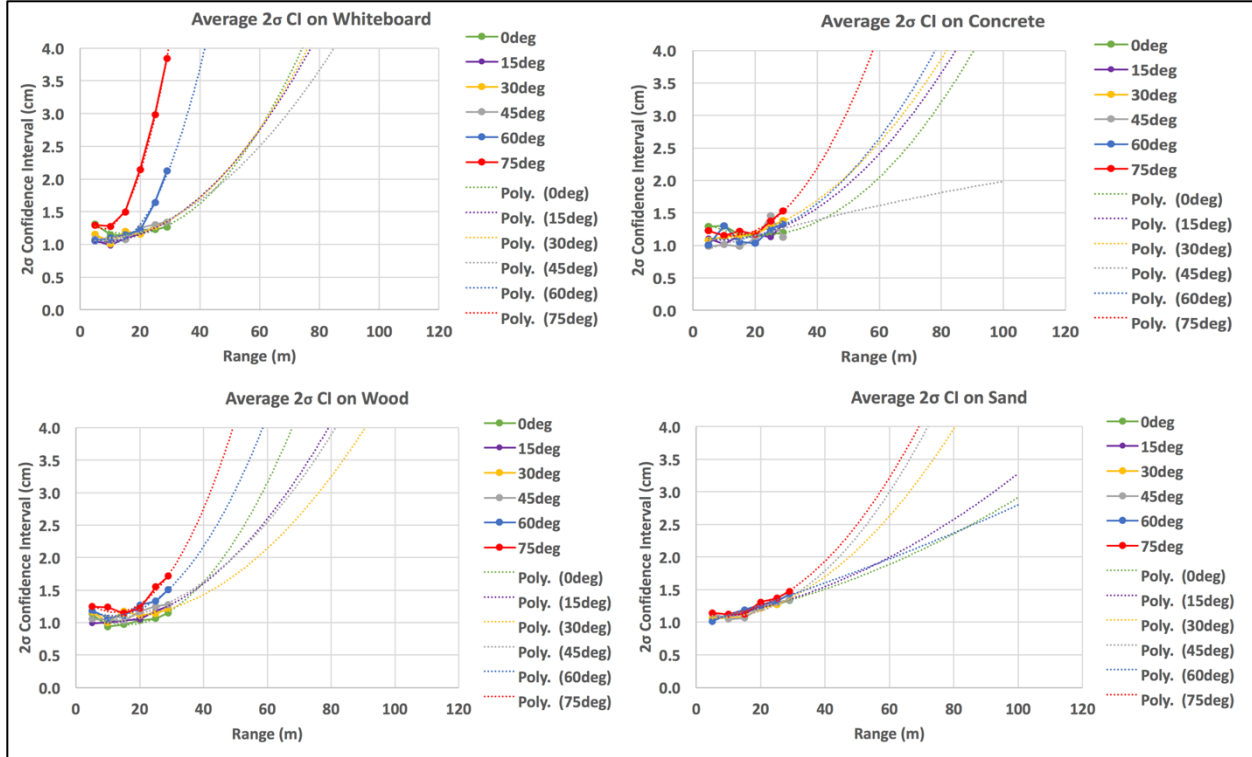


Figure 4.12: Range uncertainty results extrapolated out to the maximum range of the laser scanner, 100 m.

The range uncertainties for the remaining fifteen laser beams were estimated in a separate abbreviated experiment. When compared to the original experiment, a different target was used (a strip of aluminum), only normal incidence was observed, and only at a range of ~ 8 m. Results, shown in Figure 4.13, indicate that all laser beams are performing well within the manufacturer's specifications at that range.

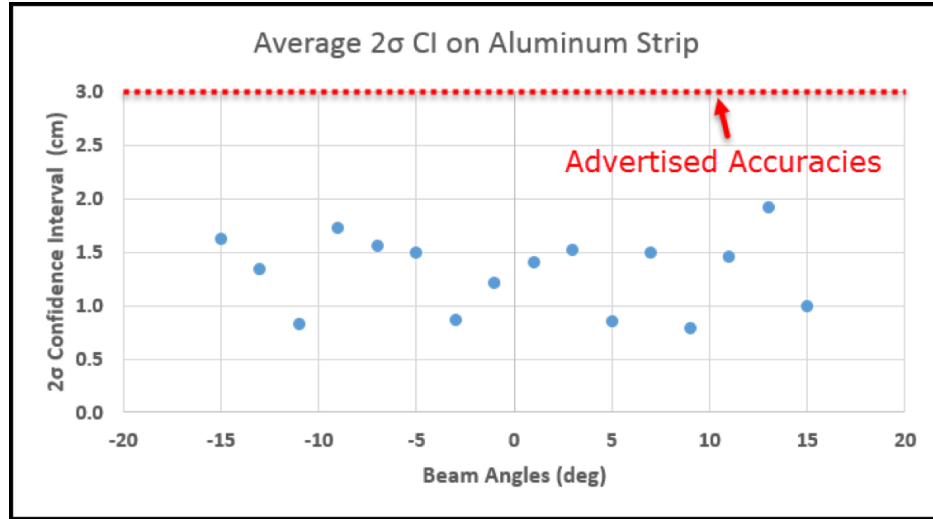


Figure 4.13: Average 2σ CI on an aluminum strip of metal at a range of 8 m and normal incidence for all laser beams.

An unexpected performance issue was observed during the data processing of the range uncertainty. The experimental configuration when using highly reflective targets at a close range and at normal incidence resulted in the intensity values of the laser measurements, within the peak value area of the target, to become saturated (i.e., maximum dynamic range value). As a result, the saturated laser measurements showed a 1-cm bias toward the scanner in the range measurements. This effect can easily be seen for the whiteboard in Figure 4.14, which shows a side view of the entire target and visually accentuates the range bias. This effect is most likely due to the digital-signal processing for ranging threshold selection such as the leading edge of the pulse or at a specific fraction of the signal peak (Baltsavias 1999).

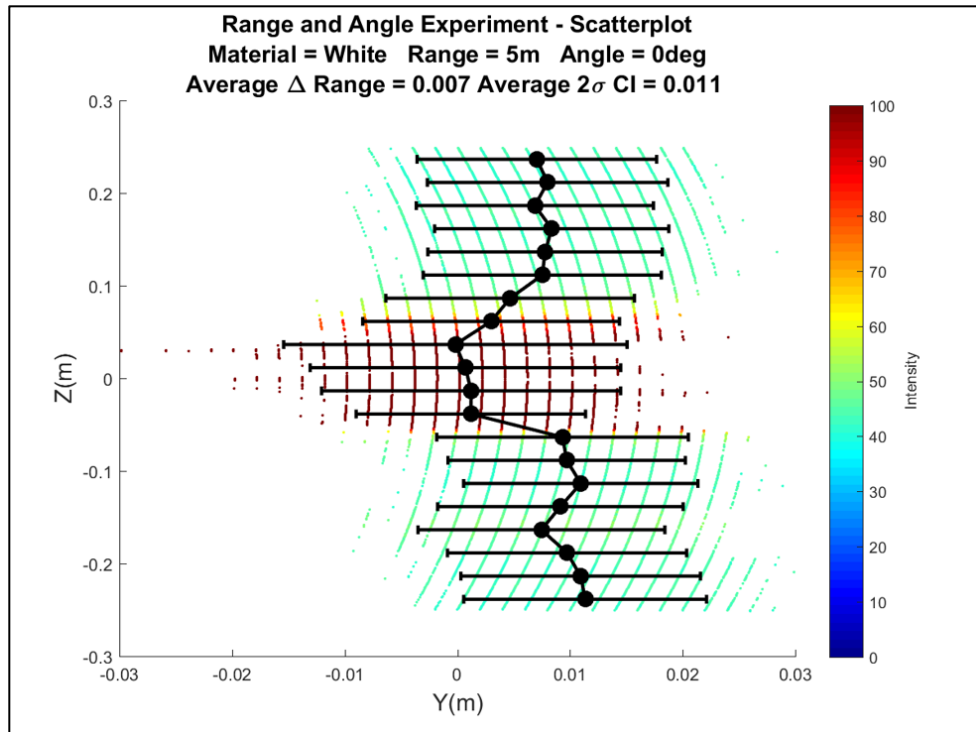


Figure 4.14: Side-view of the range bias observed due to oversaturated data points with respect to intensity within the specular area of the target.

aaa

Data Density

Data density in the spatial domain was assessed by running computer simulations with various scanner configurations (i.e., orientation of scanner and scan rate) at a given vessel speed. The scanner configurations and vessel speed used in the simulations are based on realistic field conditions. It is important to note that a field validation of the results was conducted, however it was unrealistic to maintain constant vessel speed and heading due to wind, waves, and currents. The data density in the simulation was calculated for target distances ranging from 10-100 m at 10 m intervals with a vessel speed of 4 kt (2 m/s) at scanning rates of 5 Hz and 20 Hz. Figure 4.15 and Figure 4.16 show the results of the laser scanner computer simulations with the scanner mounted in two orientations: vertically and with a 45° pitch-angle forward, respectively. For visual purposes that were not used in the calculations, noise in the form of realistic vessel rotations (roll, pitch, yaw) was introduced to the simulation plots using a randomly generated multiplier so that the scanning patters didn't perfectly align. Table 4.3 summarizes the total laser measurement count within a 1 m² window at various configurations. The laser point measurement count did not include any random vessel rotations.

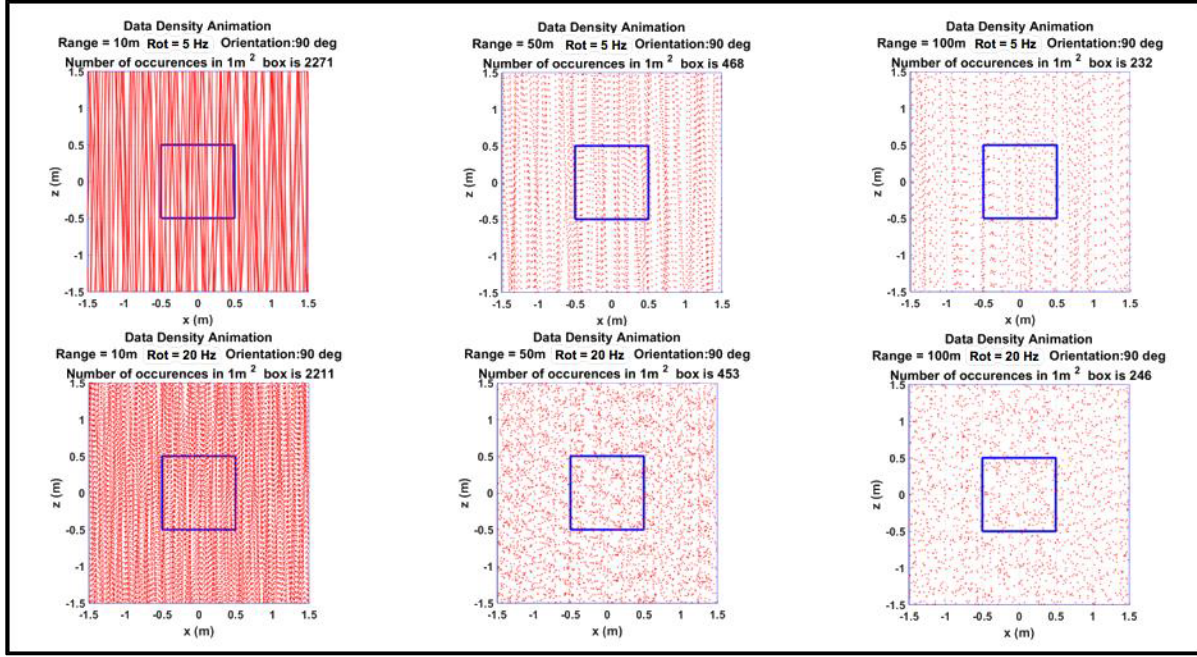


Figure 4.15: Data density simulations for targets at 10 m (left), 50 m (center) and 100 m (right) using 5 Hz (top) and 20 Hz (bottom) scanning rates with the scanner mounted vertically. The blue window represents the 1 m² target used to estimate data density.

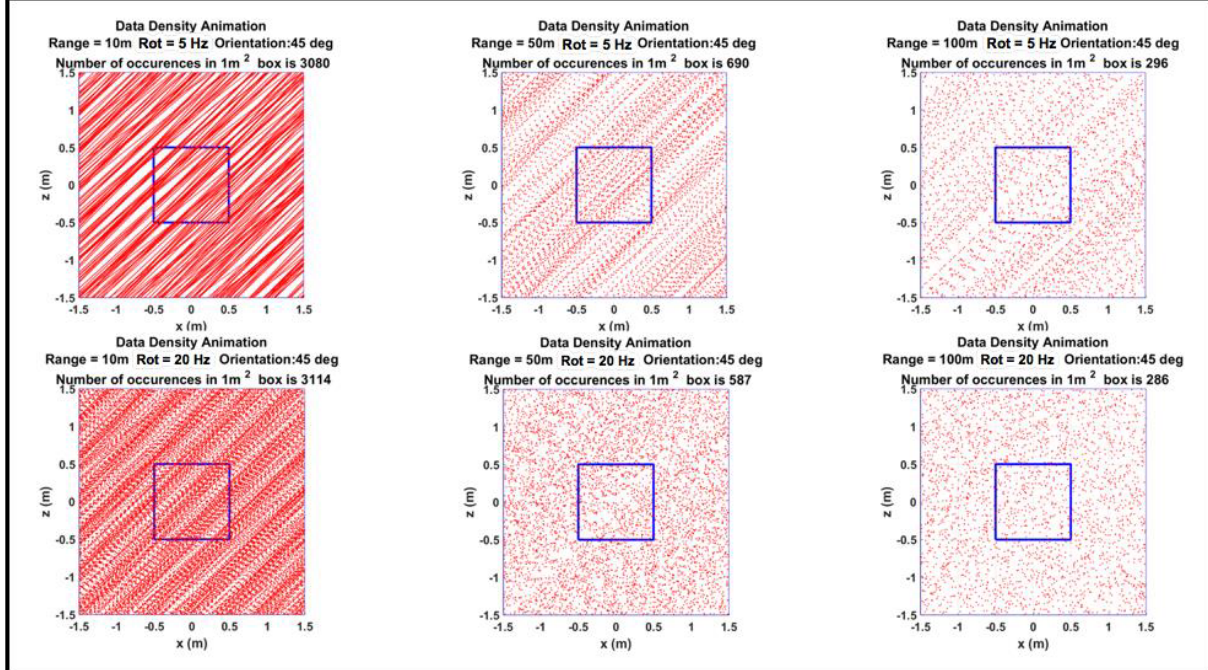


Figure 4.16: Data density simulations for targets at 10 m (left), 50 m (center) and 100 m (right) using 5 Hz (top) and 20 Hz (bottom) scanning rates with the scanner mounted at an oblique 45deg angle. The blue window represents the 1 m² target used to estimate data density.

	Vertical Scan (pt/m ²)		Oblique Scan (pt/m ²)	
Range (m)	5 Hz	20 Hz	5 Hz	20 Hz
10	2186	2333	3146	3158
20	1102	1080	1580	1583
30	722	780	1050	1029
40	600	471	797	820
50	418	468	644	644
60	360	471	515	560
70	396	465	440	411
80	238	156	396	369
90	259	157	350	335
100	190	157	326	308

Table 4.3: Results of the point count within a 1 m² window from the data density simulation

The same scanner configurations used in the simulation were also used in the data density field validation experiment. The intended speed of advance of the R/V Gulf Surveyor vessel throughout the survey was 4 kt (2 m/s), though, this was difficult to maintain due to the presence of a strong ebb current. In addition, it was also difficult to maintain a parallel heading with respect to the pier face and as a result, some of the configurations were not perpendicular to the target. Due to a strong ebb current at the very end of the field data collection, a +5°-10° heading vector was needed to maintain a course-over-ground vector that was parallel to the pier-face.

Figure 4.17 shows the rotated data point cloud and the 1 m^2 blue window used to estimate point density in the spatial domain.

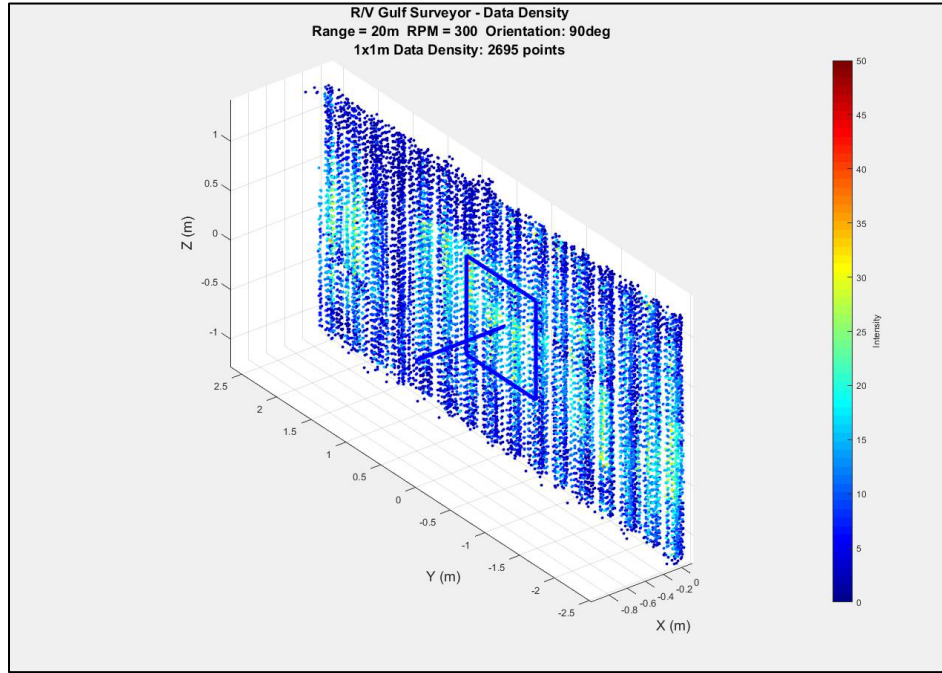


Figure 4.17: Data density results within a 1 m^2 window (marked in blue) at a range of 20m, scanner rotation rate of 5 Hz with a vertical scanner mounting orientation. The blue line represents the normal vector from the plane-of-best-fit used to align the box and plane of data.

Table 4.4 shows the results of the point count within a 1 m^2 window from the data density field validation experiment. Due to the nature of the field experiments, the point count results contain the signal from vessel motion, both rotational and translational.

Range (m)	Vertical Scan (pt/m ²)		Oblique Scan (pt/m ²)	
	5 Hz	20 Hz	5 Hz	20 Hz
10	1808	2107	1499	1825
20	1099	963	1190	1348
30	697	622	913	758
40	522	445	708	528
50	287	277	421	339
60	99	286	206	246
70	73	157	137	137
80	27	142	54	19
90	38	21	0	1
100	12	12	2	0

Table 4.4: Tabular results of the point count within a 1m² box from the field validation experiment

A comparison was conducted by computing the percent error between experimental and theoretical results using Equation 4.1. Results from said comparison are presented in Table 4.5.

$$\text{Equation 4.1: } \%_{\text{error}} = \left| \frac{\#_{\text{experimental}} - \#_{\text{theoretical}}}{\#_{\text{theoretical}}} \right| * 100$$

Range (m)	Vertical Scan (pt/m ²)		Oblique Scan (pt/m ²)	
	5 Hz	20 Hz	5 Hz	20 Hz
10	17.3	9.7	52.4	42.2
20	0.3	10.8	24.7	14.8
30	3.5	20.3	13.0	26.3
40	13.0	5.5	11.2	35.6
50	31.3	40.8	34.6	47.4
60	72.5	39.3	60.0	56.1
70	81.6	66.2	68.9	66.7
80	88.7	9.0	86.4	94.9
90	85.3	86.6	100.0	99.7
100	93.7	92.4	99.4	100.0

Table 4.5: Percent error between theoretical (computer simulation) and experimental (field validation). Small numbers represent a good comparison and large numbers represent a poor comparison.

Generally, there is a relatively good comparison between theoretical and experimental values at close ranges, 10-40 m, and poor comparison at far ranges, 50-100 m. There are a few reasons why the percent error between theoretical and experimental are so high, especially at longer ranges. As mentioned in the methodology section, the computer simulations evaluated only the geometrical ray path of the laser scanner. The simulations did not include any sources of

radiometric losses from the environment, for example, absorption and scattering losses, beam divergence, and target reflectivity. This can be easily seen in the percent error calculations at far ranges where the effects of radiometric losses are maximized. This is also why the theoretical numbers overestimate the field density data. Additionally, the effects of vessel motion are not accounted for in the experimental data.

5. Discussion

Field Operations

NOAA's mission of hydrographic survey for nautical charting, is carried out by a hydrographic fleet of four ships: NOAA Ship *Rainier*, NOAA Ship *Fairweather*, NOAA Ship *Thomas Jefferson*, and NOAA Ship *Ferdinand R. Hassler*. In addition to the capabilities of the ships themselves, these survey vessels carry thirteen smaller launches and jet-boats also equipped with sensors required to complete bathymetric surveys. It is on these smaller platforms that the use of mobile laser scanners for surface feature mapping is envisioned to be utilized. By integrating the TLS into the acoustic survey system, the vessel can conduct calibration, data collection, and data processing in concert with the *in situ* acoustic systems. Due to the gradual slope of the seabed along the Atlantic coastline, characteristic to passive continental margins, shoreline features that are exposed are often found well within the 4-meter contour and NALL, which under NOAA's present operational guidelines are not required to be surveyed. Exceptions to this generalization exist in the northern New England area and within the ports and harbors. In these settings, several interesting types of surface features were identified:

Vegetation and Surface Ripples

It was apparent that the TLS was particularly sensitive to vegetation floating in the water. If the vessel passed by an area where there was seaweed floating in the water, the scanner would easily detect the vegetation, especially dense mats but also sparse fragments. Marine navigation

authorities note that the presence of kelp on the surface generally means there are submerged rocks within that area (NOAA 2017). For this reason, NOAA hydrographers often delineate kelp areas on nautical charts, usually annotating the area by drawing the area by hand on a chartlet at the time of data acquisition. It is possible to improve upon current methods for mapping vegetation using the TLS, though the distribution and position of kelp beds are highly variable in a temporal sense due to the relatively fast growth rates and the effects of current on the horizontal position of the upper canopy. It was also observed that the TLS easily detected the water surface around the survey vessel out to a variable distance depending on the presence and size of wind-induced capillary waves.

Other than noise created by the oversaturation of the sensor by the direct path or reflections of the sun, the detection of debris and/or vegetation on the water surface, and the detection of the water surface adjacent to the survey vessel, the Velodyne VLP-16 generates relatively clean point clouds and needs very little cleaning. The acquisition software used, Hypack, allows the user to filter the data in real-time by establishing minimum and maximum ranges and/or angle sectors. This ability allows the user to prevent much of the unwanted data from ever being recorded which cuts down on the post-processing time required to yield cleaned point clouds. The following figures (Figure 5.1 - Figure 5.8) are of prominent features found within Portsmouth Harbor in addition to a few representative areas along the rocky shoreline.



Figure 5.1: Whaleback Lighthouse at the entrance to Portsmouth Harbor. Scanning range to lighthouse was approximately 70 m.



Figure 5.2: Rocky islet at the entrance of Portsmouth Harbor. Scanning range to right-most rock was approximately 64 m.



Figure 5.3: Pilings and floating pier near Fort Point, NH.

Bridges and Overhead Power Cables

The TLS performed well on both bridges and overhead power cables that were surveyed in Portsmouth Harbor, NH. Data densities sufficient to measure characteristic dimensions (vertical and horizontal clearances) were achieved in one or two passes along the features with exception to the I-95 overhead power cables. Due to the relatively small diameter of the Aluminum Conductor Steel Reinforced (ACSR) cable (1.8 cm) and the range from the TLS near the water surface to the cable of ~ 50 m, multiple passes were required in order to confidently determine the vertical clearance of the feature. The multiple passes required still only took a few minutes to acquire. Even with multiple passes, data on the upper ACSR cables were not able to be collected, however, the radar reflectors on the upper cables were strong enough targets which allowed the estimation of the cable range from the scanner, ~ 90 m. The combination of target reflectivity and target area within the laser beam footprint likely cannot have satisfied the criteria presented by Baltsavias, such that if a TLS is capable of measuring the distance to a flat and even surface area, A, with a reflectivity of $\rho=5\%$, then the minimum area of a detectable object with a reflectivity $\rho=100\%$ at the same distance would be $A/20$.

The point clouds of the Memorial Bridge (Figure 5.4), Sarah Mildred Long Bridge (Figure 5.5), I-95 Bridge (Figure 5.6), Backchannel overhead power cables (Figure 5.7), and I-95 power cables (Figure 5.8) are shown below.

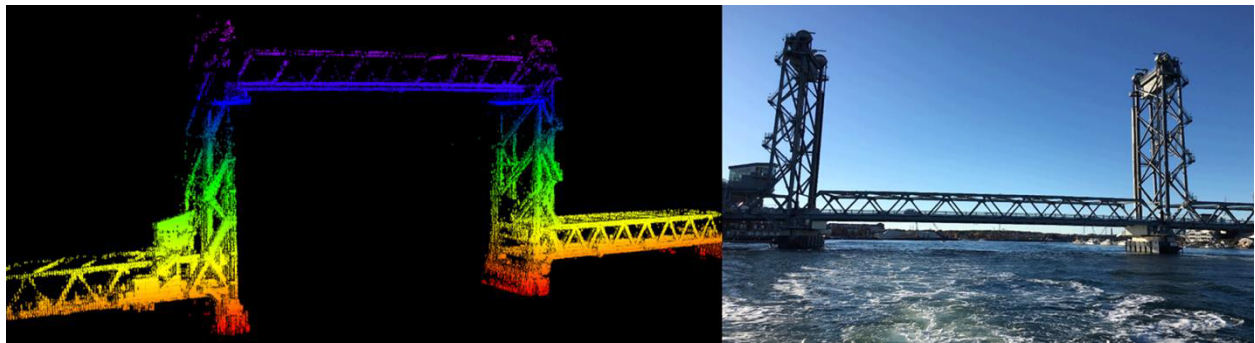


Figure 5.4: Memorial Bridge within Portsmouth Harbor. Scanning range to bottom of bridge span was approximately 60m.

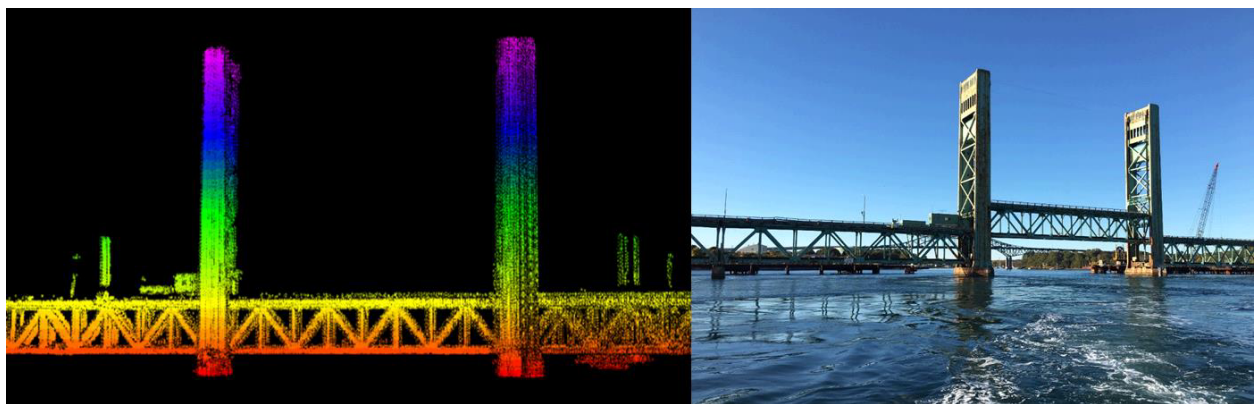


Figure 5.5: Sarah Mildred Long Bridge within Portsmouth Harbor. Scanning range to top of the pillars was approximately 75m.

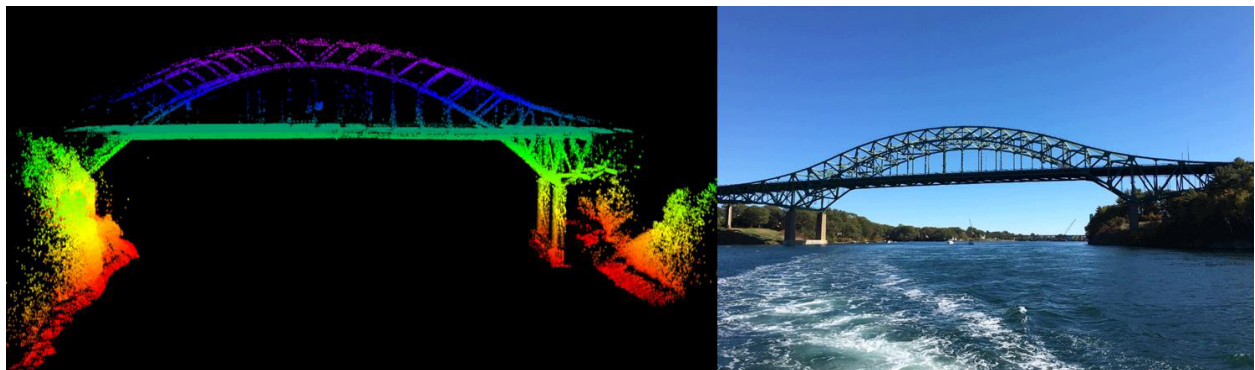


Figure 5.6: I-95 bridge within Portsmouth Harbor. Scanning range to the bottom of the bridge span was approximately 60m.

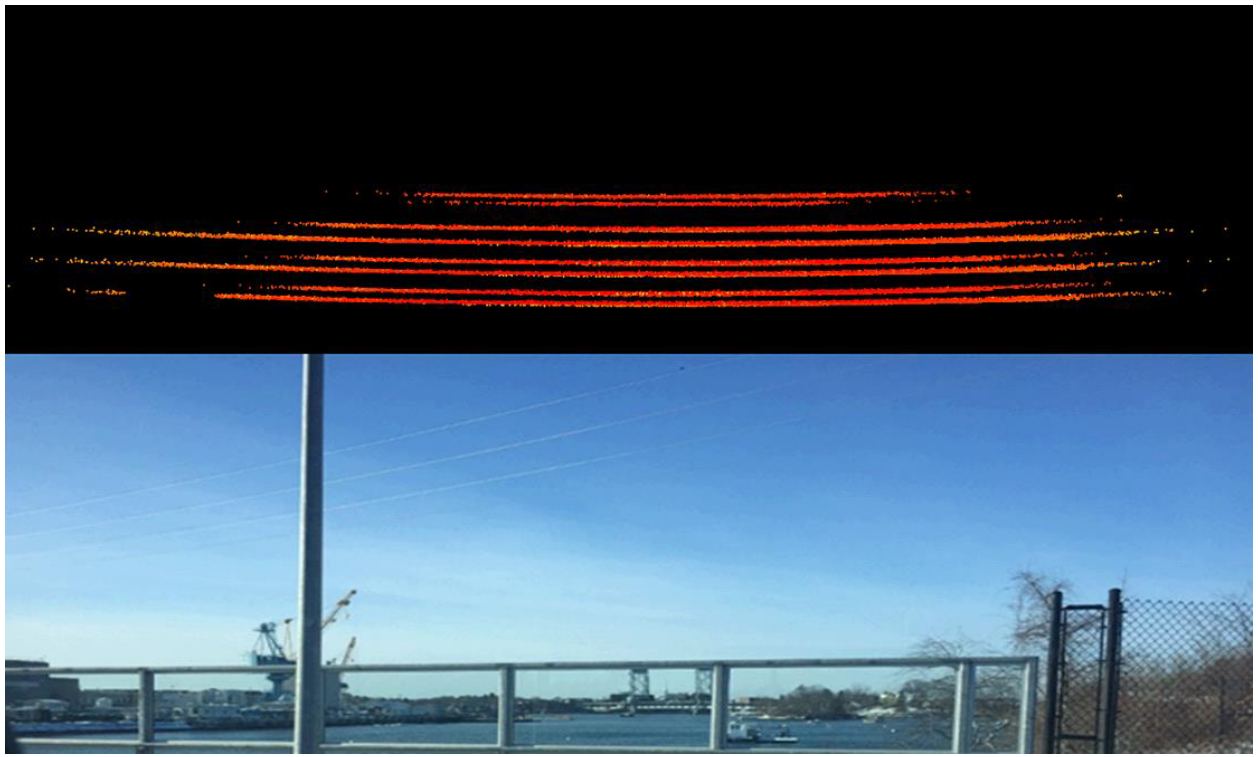


Figure 5.7: Overhead power cables stretching across Back Channel area within Portsmouth Harbor. Range to cables was approximately 16m.

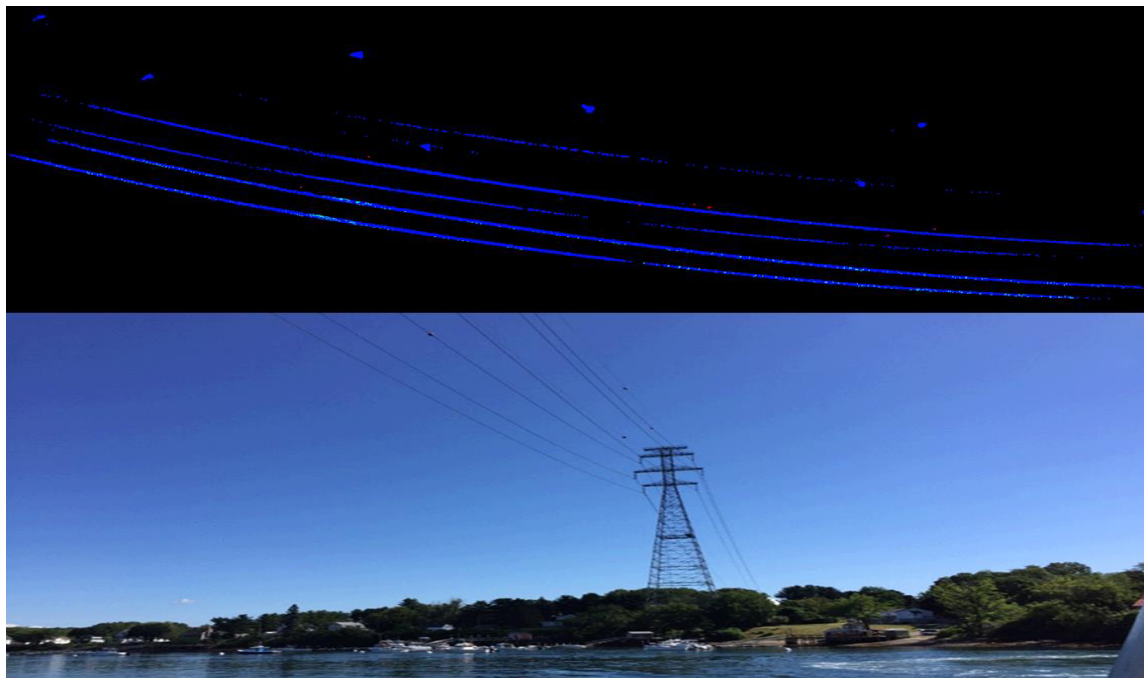


Figure 5.8: Overhead power cables stretching across the main channel just north of the I-95 bridge within Portsmouth Harbor. Range to cables was approximately 60m.

Vertical clearances of features that span the main navigational channel are of high importance to mariners. This is particularly true for vessels of which the draft drastically changes depending on the cargo loaded aboard. Captains often are required to wait for an appropriate height of tide before they can commence approaching a harbor via passing under a bridge due to air gap limitations. An air gap is the vertical distance from the lowest part of a feature down to a chart datum. For NOAA charts, this height datum is referenced to Mean High Water (MHW). The charting authority for vertical clearances of overhead features is the USCG Bridge Office. In October 2010, the United States Army Corps of Engineers (USACE) contracted a commercial survey company to survey twenty-two bridges on the Ohio River in order to update vertical clearances with suspected discrepancies. Survey results showed an average discrepancy of 5.2 ft with a maximum discrepancy of 11.6 ft lower than the published vertical clearance on the I-24 Highway Bridge. The USACE have developed new policy and procedures in collaboration with the USCG Bridge Office. The USCG now accepts updated vertical clearance values generated from laser scanner surveys which in turn allows the USACE to update their charts. Currently, no policy or procedure exists between NOAA and USCG which permits NOAA to perform similar updates for vertical clearances of overhead features.

The vertical clearances of the overhead features surveyed within Portsmouth Harbor, NH with the Velodyne VLP-16 were compiled by reducing the ellipsoidal heights of the point cloud to the Mean High Water datum using the local V-datum ellipsoid separation model. These values, along with the charted vertical clearances, are presented in Table 5.1. Resulting differences could be due several reasons including inaccurate boresight calibration, thermal expansion/contraction of power cables, environmental changes sense the initial survey was

completed, or inaccurate initial survey results. Without an independent and current repeat survey, reasons for differences are unable to be determined.

Feature	Charted VERT CL (m)	Surveyed VERT CL (m)	Difference (m)
Memorial Bridge, open	45.7	44.5	1.2
Memorial Bridge, closed	6.4	5.3	1.2
Sarah Mildred Long Bridge, open	41.1	40.6	0.5
Sarah Mildred Long Bridge, closed	3.0	1.4	1.6
I-95 Bridge	40.8	39.7	1.2
I-95 Power cables	50.2	52.9	-2.7
Backchannel Power cables	19.8	18.1	1.7

Table 5.1: Charted vs. surveyed vertical clearances of overhead features surveyed within Portsmouth Harbor, NH. Difference = charted - surveyed

Compliance with IHO's S-44 Standards

The results of the performance analysis of the Velodyne VLP-16 shows that the TLS is a capable tool for conducting shoreline survey operations that meet IHO S-44 standards. Following all the potential capabilities mentioned above, it should be also noted that the performance of the laser scanner system can be negatively impacted by certain environmental conditions. One issue that became immediately apparent with using the TLS was the effects of the direct path of the sun within the IFOV of the sensor. When this occurs, or when the sun's rays are reflected off a specular surface, such as a smooth water surface without any capillary waves, the signal becomes saturated within that region of scan angles and the data becomes unusable. Considering this

effect, the best time of day in which to conduct laser scanner survey is at night (Baltsavias 1999) though visual identification of targets being lased becomes problematic. Bright sunny days with flat water conditions which create specular surfaces may cause the signal to become saturated within angles (azimuths and elevations) close to parallel with the direct path to the sun and specular surface reflections. It is recommended to conduct laser scanner surveys with the sun on the opposite side of the vessel from the target of interest (Pe’eri 2009). This requirement is similar to survey requirements for Airborne LiDAR Bathymetry (ALB) operations. Without the use of filters, either as an optical component or as an algorithm in the processing software, the survey datasets are expected to contain large amounts of ‘flyers’ or false positives. The accumulation of water droplets on the lens of the scanner due to precipitation or ocean spray caused by breaking waves may also pose a challenge for the scanner. It is expected that the outgoing laser beam would be refracted or defocused enough such that the returning signal is too weak to be detected. While conditions that cause breaking waves are rarely suitable for conducting shoreline survey, high speed transits to the survey area may cause salt water spray to accumulate on the scanner. It is also expected that suspended air particles in the form of rain, fog, mist, or even haze (caused by air pollution) may negatively affect system performance.

As such, the key uncertainty sources that should be included in the performance of the laser scanner are boresight calibration and vessel offset parameters, and position, attitude, and timing parameters. The uncertainty values presented below are a first order estimate for the possible range of errors that may be expected which are presented in the NOS Hydrographic Surveys Specifications and Deliverables (HSSD) and are reported at the 68% confidence level (1σ) (NOS 2016).

The uncertainty of the boresight calibration parameters would reflect the angular uncertainty of the rotational orientation of the TLS with respect to the IMU body frame. The boresight calibration of the laser scanner was similar to the boresight calibration methods of acoustic sensors. By collecting data on a prominent feature from various directions and orientations, sensor rotations (roll, pitch, yaw) were adjusted until the point cloud residuals were visually minimized. According to the HSSD, commonly reported values of the boresight calibration uncertainty are less than 1°. The uncertainty of the vessel offsets is 0.001-0.1 m. The uncertainty of the positioning solutions will largely depend on the method of positioning used such as Differential Global Positioning System (DGPS), Post Processed Kinematic (PPK), or Real-time Kinematic (RTK) but are usually reported at 1m. The uncertainty of the rotational attitude parameters (heading (gyro), pitch, and roll) are commonly reported at 0.02° while the translational attitude parameter, heave, is 5% of the heave amplitude or 0.05 m, whichever is greater. The timing uncertainty is usually 0.005-0.01 seconds which is used for the timing of all navigation sensors; gyro, heave, pitch, and roll. Based on the study results, the performance of the industrial-grade TLS is operating well within the uncertainty budget to meet IHO S-44 standards.

Future Directions

In order to provide better results in estimating data density by running computer simulations, sources of radiometric losses from the environment should be incorporated, for example, absorption and scattering losses, beam divergence, and target reflectivity. Uncertainty models

should be created to incorporate uncertainty from sources such as boresight calibration parameters, position and attitude parameters, and environmental parameters to assign uncertainty values to each data point in real-time. Boresight calibration techniques that do not require the presence of an ‘ideal target’ such as a pier face and/or day marker should be investigated. If the deployment of these TLS on marine survey vessels is necessary in remote locations without features such as these, such as in remote areas of Alaska, current boresight alignment procedures by scanning a target from various directions and orientations and aligning the point clouds could be impractical.

6. Conclusions

The current methods of conducting NOAA traditional shoreline survey can be vastly improved by implementing a low-cost industrial-grade mobile laser scanner. Past studies have proved that conducting shoreline survey operations using a survey-grade TLS provide more accurate deliverables, take less time to complete, and is safer for the survey crew deployed in the field in comparison to traditional shoreline survey methods.

In this work, it has been demonstrated that an industrial-grade TLS can be used to conduct shoreline surveys operation that meet IHO S-44 specifications. As part of a field evaluation, it was shown that the TLS can be used for measuring air gaps of overhead features and heights of non-contiguous features that are above the water surface.

Several components of the TLS were independently verified in a well-controlled environment. By conducting a series of laboratory experiments, it was demonstrated that the laser beam elevation angles have an average uncertainty of 0.06° but are generally well-aligned throughout the $\pm 15^\circ$ vertical FOV. Additionally, it was demonstrated that the uncertainty of the ranging estimates is dependent on range and angle of incidence on various target types. The study results did show that the range uncertainties were within the manufacturers specifications (1.5 cm) at a limited range of 30 m. A combination of computer simulations that mimicked the physical characteristics and geometrical configuration of the TLS and a field validation dataset were used to evaluate the data density potentials of the scanner. It was shown that at close ranges the TLS is expected to generate extremely dense point clouds ($\sim 2,000 \text{ pt/m}^2$). However, the effects of

vessel motion and radiometric losses limit the data density potential at far ranges, particularly at ranges > 80 m.

The implementation of these low-cost industrial-grade mobile laser scanners aboard marine survey vessels improves upon traditional NOAA shoreline survey methods which will yield more accurate deliverables, take less time to complete surveys, and is safer for the survey crew deployed in the field. With that said, the greatest environmental challenge for the Velodyne VLP-16 is the effect of the direct path of the sun or reflections from specular surfaces that cause false positives. In general, these data artifacts are easy to clean, except for when the target of interest is between the path of the scanner and the light source.

References

- Baltsavias, E. P. 1999. "Airborne Laser Scanning: Basic Relations and Formulas." *ISPRS Journal of Photogrammetry and Remote Sensing* 54 (2–3): 199–214. doi:10.1016/S0924-2716(99)00015-5.
- Brennan, Richard, Peter Canter, Jim Van Rans, and Antonio Silva. 2008. "Surface Imaging Capabilities on Marine Hydrographic Vessels." *Hydro International* 12 (1): 14–17.
- Bunkin, A, and K I. Voliak. 2001. *Laser Remote Sensing of the Ocean: Methods and Applications*. Vol. Vol. 56.
- Fossen, Thor I. 2011. "Handbook of Marine Craft Hydrodynamics and Motion Control." John Wiley & Sons, Ltd. <http://onlinelibrary.wiley.com/book/10.1002/9781119994138>.
- Gonsalves, Michael O. 2010. "A Comprehensive Uncertainty Analysis and Method of Geometric Calibration for a Circular Scanning Airborne Lidar." *PhD Proposal*. doi:10.1017/CBO9781107415324.004.
- Habib, Ayman, Ki In Bang, Ana Paula Kersting, and Jacky Chow. 2010. "Alternative Methodologies for LiDAR System Calibration." *Remote Sensing* 2 (3): 874–907. doi:10.3390/rs2030874.
- IHO. 2008. "IHO Standards for Hydrographic Surveys - Special Publication No. 44." International Hydrographic Bureau. doi:10.1017/CBO9781107415324.004.
- Kovalev, V. A. 2004. *Elastic Lidar : Theory, Practice, and Analysis Methods*.
- Mallace, Duncan, and John Dillon-Leetch. 2008. "Multibeam and Laser: Combined High Resolution Hydrographic Surveying for Civil Engineering Project Support," 1–15.
- Maune, David F. 2007. *Digital Elevation Model Technologies and Applications: The DEM Users Guide*.

- Manual*. 2nd Editio.
- Measures, R. M. 1992. *Laser Remote Sensing: Fundamentals and Applications*. 2nd Editio.
- National Electrical Manufacturers Association. 2004. “Degrees of Protection Provided by Enclosures (IP Code),” 8. www.nema.org.
- NOAA. 2017. *Coast Pilot 7*. Vol. 49.
- NOS. 2016. “NOS Hydrographic Surveys Specifications and Deliverables.” U.S. Department of Commerce, National Oceanic and Atomospheric Administration.
http://www.nauticalcharts.noaa.gov/hsd/specs/HSSD_2016.pdf.
- OSHA. 2016. “OSHA Technical Manual.” Accessed December 10. otm_iii_6 @ www.osha.gov.
- Parrish, Christopher E. 2012. “Shoreline Mapping.” In *Advances in Mapping from Remote Sensor Imagery: Techniques and Applications*. Boca Raton, Florida: CRC Press, Taylor and Francis Group.
- Pe’eri, Shachak. 2009. “Surface Analysis,” no. Oe 875: 666. doi:10.1002/9780470721582.
- . 2015. “Performance Evaluation (Airborne Lidar Bathymetry).”
- Pradith, Vitad, Shachak Pe, David Maddock, David Oroshnik, and Jack Riley. 2015. “Integrating Industrial Laser Scanners for Small Vessel Operations,” 1–6.
- THORLABS. 2016. “High-Precision Rotation Mount,” 4–5.
https://www.thorlabs.com/newgroupage9.cfm?objectgroup_id=2464.
- Vanicek, Petr, and Edward J. Krakiwsky. 1986. *Geodesy: The Concepts, Second Edition*. 2nd Editio. Elsevier Science Publishers B.V.
- Velodyne LiDAR. 2015. “VLP-16 User’s Manual and Programming Guide.” Velodyne LiDAR.
- Wehr, Aloysius. 2008. “LiDAR Systems and Calibration.” In *Topographic Laser Ranging and Scanning*. doi:10.1017/CBO9781107415324.004.

Wehr, Aloysius, and Uwe Lohr. 1999. "Airborne Laser Scanning - an Introduction and Overview." *ISPRS Journal of Photogrammetry and Remote Sensing* 54 (2–3): 68–82.
doi:Doi: 10.1016/s0924-2716(99)00011-8.

Wyllie, Katrina, Grant Froelich, Karen Cove, and Karen Hart. 2012. "Process for Capturing Real World Features from 3D Laser Scanned Point Clouds." In .